ADVANCED FUNCTIONAL MATERIALS
www.afm-journal.de

Exploring the Properties of Disordered Rocksalt Battery Cathode Materials by Advanced Characterization

*Roujia Chen, Chu Lun Alex Leung, and Chun Huang**

Cation-disordered metal oxides as cathode materials for Li ion batteries have been overlooked from early studies due to to the restriction of Li ion diffusion, leading to poor electrochemical performance. However, the discovery of a new disordered rocksalt (DRX) structured material $Li_{1.211}Mo_{0.467}Cr_{0.3}O_2$ with a high capacity of >260 mAh g^{-1} at 0.05 C opened new research prospects in this emerging field and established DRX materials as a promising alternative with wider choices of transition metal elements compared with currently widely used layered cathode materials. Some of the major obstacles of the DRX materials include γ-$LiFeO_2$ type cation short-range-order that impedes Li ion diffusion, irreversible oxygen loss, and transition metal dissolution, which also present challenges for appropriate characterization techniques. Several performance optimization strategies have been employed, including fluorine incorporation, high entropy modification, and surface coating. This review article focuses on advancements in characterization techniques to uncover underlying mechanisms of Li ion diffusion and degradation of the DRX cathode materials to address the abovementioned challenges and provide inspiration for future studies of this class of materials.

1. Introduction

Although the energy density of Li ion batteries (LIBs) has been steadily increasing, there exists a broad variety of electrode materials that are not fully explored yet. The recent advancements in cation disordered rocksalt (DRX) cathodes have demonstrated new imagination space over the utilization of inexpensive transition metals (TMs) as raw materials to replace Co and Ni in existing cathode materials and offer high specific capacities and energy that can advance toward more sustainable LIBs[1] (**Figure 1a,b**).[2–5]

Unlike conventional intercalation cathode materials with an α-$NaFeO_2$-type structure where 2D Li transport occurs between TM layers, the mixing of cations (Li and TM) is observed in the cation DRX type cathodes, which adopt a α-$LiFeO_2$-type structure[6] (Figure 1c). The DRX materials had long been neglected as a good cathode material, as cation mixing was believed to restrict effective Li transport, and poor electrochemical performance.[7] However, the early report of a high capacity (>260 mAh g^{-1} at 0.05 C) for the DRX $Li_{1.211}Mo_{0.467}Cr_{0.3}O_2$ (LMCO) material[7] unlocked the potential research space. Later studies show some of the DRX materials possess higher theoretical capacities (up to 425 mAh g^{-1}) and energy densities (up to 1200 Wh kg^{-1}) compared to existing ordered cathode materials, e.g. ≈220 mAh g^{-1} and 800 Wh kg^{-1} for $LiNi_xMn_yCo_zO_2$ (NMC) owing to the energy storage contributions from excess Li and both TMs and O-redox that increase capacity,[3,4] making DRX materials a promising alternative to layered and olivine structured cathode materials.

Among all rocksalt-typed crystals, there exists stoichiometric octahedral holes (Oh) and tetrahedral holes (Td) in the lattice (**Figure 2**). For Li migration process in the conventional layered crystal structure, Li ions alternate through Oh to Td to Oh, known as the o-t-o diffusion. In DRXs, 5 different environments can be found according to different cation mismatches and arrangements, 0-TM, 1-TM, 2-TM, 3-TM, and 4-TM local environments, corresponding to Li_4, Li_3TM, Li_2TM_2, $LiTM_3$, and TM_4 tetrahedral clusters, respectively.[2] Effective Li transportation is mainly via 0-TM channels, i.e., through the connected Li_4 clusters to enable Li ion mobility.[2] The presence of 0-TM diffusion channel is a unique characteristic of DRXs, which is not found in the pristine layered materials as no cation mismatch is observed. Crystal structure and Li ion transport experiments and simulations

R. Chen, C. Huang
Department of Materials
Imperial College London
London SW7 2AZ, UK
E-mail: a.huang@imperial.ac.uk
C. L. A. Leung
Department of Mechanical Engineering
University College London
London WC1E 7JE, UK
C. L. A. Leung, C. Huang
Research Complex at Harwell
Rutherford Appleton Laboratory
Didcot OX11 0FA, UK
C. Huang
The Faraday Institution
Quad One
Becquerel Ave, Harwell Campus, Didcot OX11 0RA, UK

The ORCID identification number(s) for the author(s) of this article can be found under https://doi.org/10.1002/adfm.202308165

DOI: 10.1002/adfm.202308165

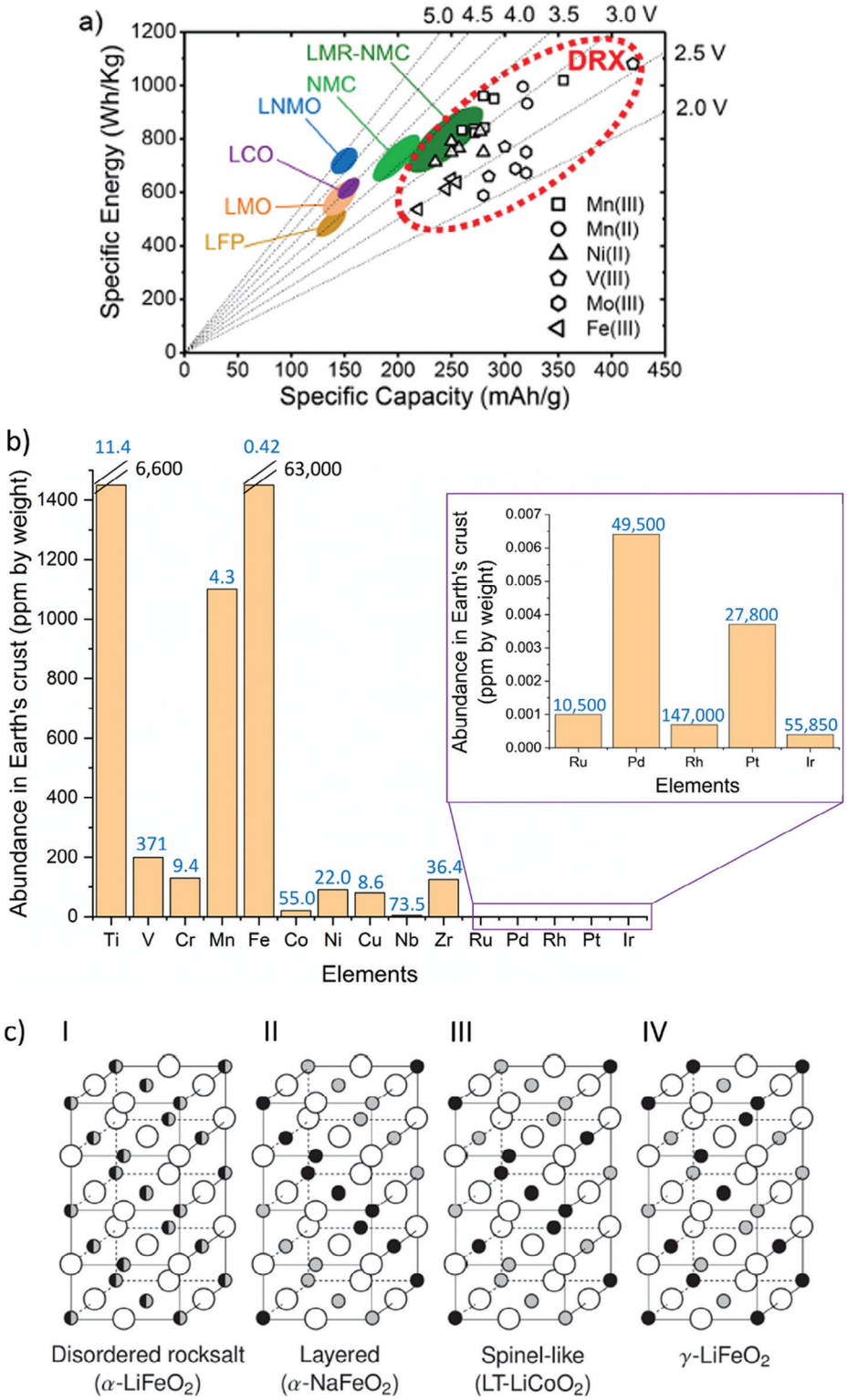

Figure 1. a) Comparing the specific energy and specific capacity of different cathode materials with those of DRXs. Adapted with permission.[8] 2021, American Chemical Society. b) The natural abundance of metals in the earth's crust and the price of each metal in USD kg^{-1} (shown in the blue figures on top of each bar). Adaptedwith permission[2–5] 2023, U.S. Geological Survey. c) Schematics of crystal structures for (I) the disordered rocksalt α-$LiFeO_2$ structure in which all cation sites are equivalent, (II) the layered α-$NaFeO_2$ structure, (III) the spinel-like low-temperature $LiCoO_2$ (LCO) structure, (IV) the γ-$LiFeO_2$ structure. Large empty circles indicate oxygen sites and small gray and black filled circles stand for lithium and TM sites, respectively. Adapted with permission.[6] 2014, John Wiley and Sons.

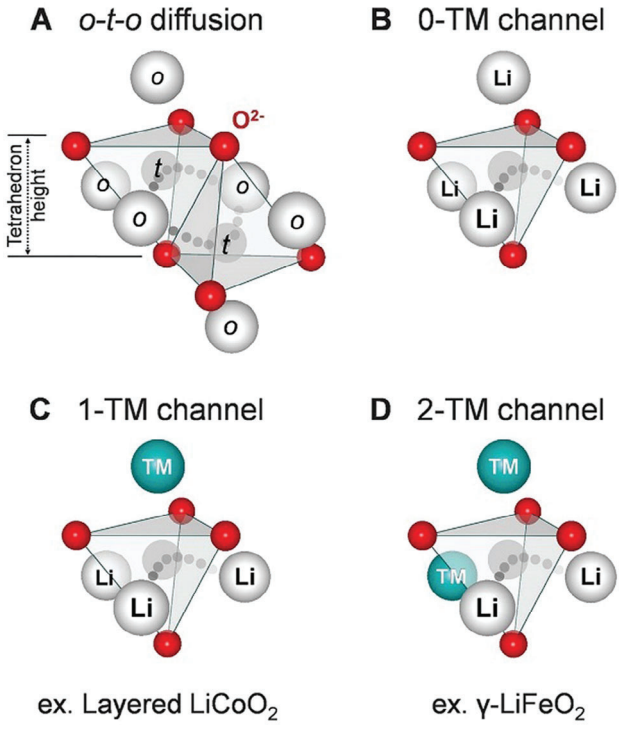

Figure 2. A) Octahedral to tetrahedral to octahedral (o-t-o) diffusion involves two tetrahedral paths that connect each pair of neighboring octahedral sites. (B to D) In the activated state, diffusion can occur through different channels depending on the number of TMs involved. The diffusion channels are categorized as follows: B) The 0-TM channel refers to diffusion where the activated state shares face with no octahedral TMs. C) The 1-TM channel corresponds to diffusion where the activated state shares a face with one TM. D) The 2-TM channel represents diffusion where the activated state shares a face with two TMs. Reproduced with permission.[7] 2014, The American Association for the Advancement of Science.

results reveal that Li-excess above 1 stoichiometry level is required to transform DRX materials to high-capacity cathodes to unlock the 0-TM percolation, e.g. it was found that a ≈10% Li-excess is required to enable 0-TM percolating network for LMCO to achieve a high capacity of 327.5 mAh g^{-1} at 0.05 C.[7] The 0-TM channels are essential for fast Li diffusion, however, the number of 0-TM channels is insufficient to form a percolating network in a non-Li-excess DRX in most cases, resulting in slow Li diffusion and poor performance in the previous studies.[2,7]

For multi-TM DRXs, only certain types of TMs contribute to the battery capacity, while metals with zero valence electrons are inactive.[9] The presence of inactive TMs (so-called compensator ions or d^0 metals, e.g. Ti^{4+}, Nb^{5+}, Ru^{5+}, Mo^{6+}) are generally smaller in size and higher in charge, which could accommodate the distorted sites in the lattice and therefore stabilize the DRXs. DRXs with multiple TMs incorporated in the structure can be referred by their active metals. For instance, in $Li_{1.25}Nb_{0.25}Mn_{0.5}O$ (LNMO),[10] the contribution to capacity is based on Mn^{3+}/Mn^{4+} redox while Nb^{5+} is the inactive d^0 metal which does not contribute to capacity, LNMO can thus be classified as a Mn-based DRX.

Density functional theory (DFT) calculations and Monte-Carlo (MC) simulations predicted a metal mixing compatibility map of high-entropy oxyfluoride cathodes which provides useful instructions for metal selection according to fundamental thermodynamics.[11] The synthesized material from 6 types of TMs ($Li_{1.3}Mn^{2+}_{0.1}Co_{0.1}Mn^{3+}_{0.1}Cr_{0.1}Ti_{0.1}Nb_{0.2}O_{1.7}F_{0.3}$) with a high configurational entropy demonstrated a desirable capacity of 307 mAh g^{-1} (955 Wh kg^{-1}) at a low rate (20 mA g^{-1}), with more than 170 mAh g^{-1} capacity retention after cycling at a high rate of 2000 mA g^{-1}.[12] The development of DRX materials also opens up compositional flexibility among earth-abundant TMs.

Currently, the performance of DRX materials is impeded by several technical challenges including low electronic conductivity of DRX particles which requires large amounts of C additives in electrode processing,[13] the lack of scalable synthesis routes to prepare high performance DRX cathodes with controlled morphologies, and the sloping voltage profiles of most DRX cathodes which creates challenges for system integration.

While there have been review articles on the DRX cathode materials, e.g. computational studies[9] and characterization techniques for batteries in general,[14] this review focuses on the recent advancements in the characterization techniques to address two major challenges of the newly emerging DRX cathode materials: (i) the presence of the γ-$LiFeO_2$-type short range order (SRO) of TM (Figure 1c) that impedes effective Li percolation in the lattice and cathode performance;[15,16,9] (ii) irreversible anionic redox and subsequent dissolution of TM cations into the electrolyte that lead to rapid reduction of battery cycling life. Both obstacles also impose significant challenges in characterization methods to study the associated underlying mechanisms as it is notoriously challenging to detect the low atomic mass Li and O which usually result in low signal-to-noise ratios.[17] This review first outlines the two significant challenges of the DRX cathode materials in Section 2, and then group various characterization techniques based on functionalities to tackle each challenge in Sections 3 and 4. Section 5 summarizes the development and applications of advanced characterization techniques that investigate the DRX materials, and provides an outlook of the aforementioned experimental approaches in the development of DRX cathodes.

2. Challenges for DRX Cathodes

2.1. Li Percolation

A recent study[15] uses DFT and MC simulations to study the local and macroscopic Li transport in two Li-rich DRXs: $Li_{1.2}Mn_{0.4}Ti_{0.4}O_2$ (LMTO) and $Li_{1.2}Mn_{0.4}Zr_{0.4}O_2$ (LMZO). The LMTO prefers forming Li_4 clusters over LMZO, indicating suppressing the γ-$LiFeO_2$ type SRO is critical in controlling Li transport environments in DRX which has a great dependence on the type of d^0 metals.[15] Various synthetic modifications have been investigated to alleviate the harmful impact of the γ-$LiFeO_2$ type SRO.

Fluorination (or F^- incorporation) has been explored to suppress γ-$LiFeO_2$ type SRO through introducing a more electronegative F^- on the O^{2-} site.[18–21] The strong bonding tendency between Li and F maximizes the Li content around F, resulting in a greater number of Li-rich clusters, thereby suppressing the γ-$LiFeO_2$ type SRO. The orthorhombic-$LiMnO_2$ (o-$LiMnO_2$) exhibits similar structural motifs to Mn-based Li-rich cathodes,[22]

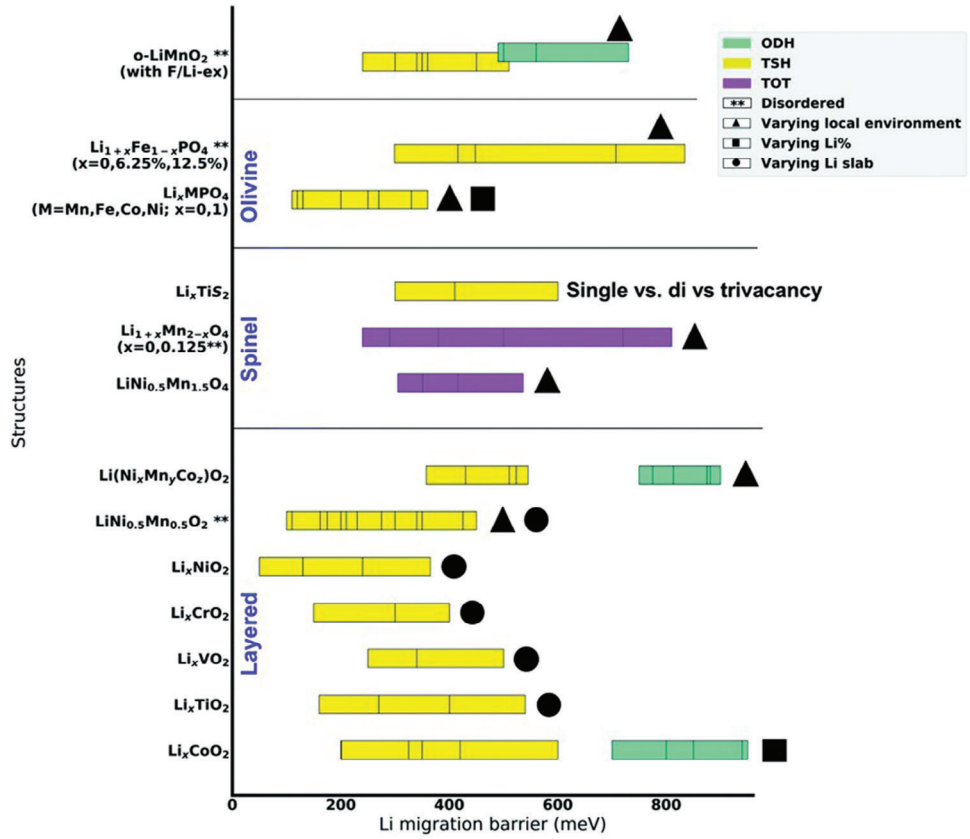

Figure 3. Comparison between activation barriers of the model system (o-$LiMnO_2$ with and without F/Li-excess) via both oxygen dumbbell hop (ODH) and tetrahedron site hop (TSH) mechanisms with available migration barriers for ODH and TSH mechanisms for various delithiated states of different layered, spinel, and olivine systems. The barriers for ODH, TSH, and o-t-o paths are shown as turquoise, yellow, and magenta bars respectively. Double stars (**) next to the name of the structure indicate a disordered structure. In the case of $Li_{1+x}Mn_{2-x}O_4$, only the Li-excess phase ($x = 0.125$) is disordered. The polygons near the bars (triangle, square, and circle) specify where variations in the barriers come from (varying local environment, Li concentration, and Li slab space, respectively). Reproduced with permission.[22] 2020, Royal Society of Chemistry.

the range of migration barriers in the model system of o-$LiMnO_2$ with and without F/Li-excess were calculated and compared with other layered, spinel and olivine systems as shown in **Figure 3**, this provides an overview of the typical migration barrier range for the materials with and without F/Li-excess and different types of cathode materials.[22]

The impact of fluorination on SRO and Li transport in DRX materials was investigated using DFT-based MC simulations.[18] **Figure 4a** shows the fraction of Li accessible by percolation in the M^{2+} systems, for all four systems, the 0-TM percolating Li amount initially decreases as F is added, but then increases at high F content, suggesting a transition from "less percolating" to "more percolating" SRO with heavy fluorination.[18] Figure 4b shows the evolution of isolated Li4 as a function of fluorination, initially the amount of isolated Li increases, at the highest F-levels there are almost no isolated Li_4 clusters, indicating that most Li is in the percolating clusters.[18] Overall, a large amount of F substitution (>15%) generally improves 0-TM percolation because Li-rich clusters around F become increasingly connected.[18] At low (<15%) F concentration, dilute F ions attract Li around them, forming yet isolated rather than percolating Li-rich domains,[9] the effects of fluorination can be beneficial or disadvantageous depending on the intrinsic SRO in the unfluorinated oxide.[18] When the origin of poor Li transport in the unfluorinated oxide is cation SRO that disfavors 0-TM percolation, fluorination enhances Li transport by disrupting these local configurations and promoting the formation of connected Li-rich environments.[18] On the other hand, if the cation SRO in the pure oxide already exhibits good 0-TM Li percolation,[7] the Li redistribution caused by small amounts of F substitution can be detrimental to 0-TM percolation as it may interrupt the existing connections between local Li-rich domains.

The highly fluorinated composition space is restricted by the F solubility limit.[23] Research in understanding the F solubility in DRX materials and how it can be manipulated through metastable synthesis routes is beneficial to the development of stable, high capacity DRX materials. For example, first-principles calculations were used to investigate the thermodynamics of fluorination in cathode materials to determine the conditions under which bulk fluorination is possible,[23] and an experiment method of using a fluorinated polymeric precursor instead of the LiF precursor was developed during synthesis of a model Li-Mn-Nb-O (LMBO) system, and increased the F content from 7.5 at% to 10–12.5 at.%.[19] Several synthesis routes targeting a highly fluorinated DRX cathode $Li_{1.2}Mn_{0.4}Ti_{0.4}O_{1.6}F_{0.4}$ were also designed and tested.[24] Precursor combinations were screened

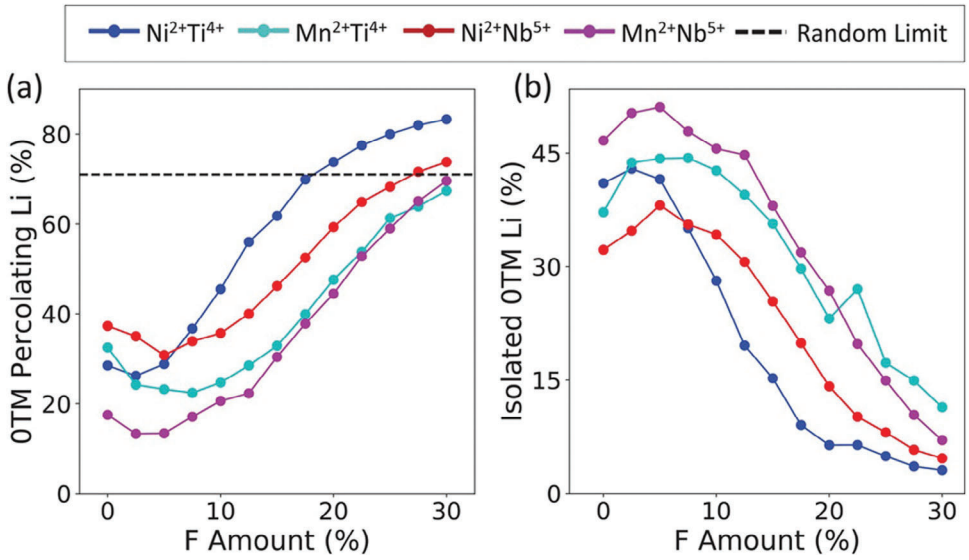

Figure 4. 0-TM percolation analysis and short-range order parameters for four types of $Li_{1.2}$ compounds obtained at 1873 K. a) 0-TM percolating Li, and b) amount of Li in isolated Li_4 as a function of F content. Adapted with permission.[18] 2020, John Wiley and Sons.

to raise the F chemical potential and avoid the formation of LiF which inhibits fluorination of the targeted DRX phase.[24] At low temperatures, MnF_2 reacts with the Li source, forming LiF, thereby trapping F in strong Li-F bonds, LiF can react with Li_2TiO_2 to form Li_3TiO_3F; however, MnO is not easily incorporated into this DRX phase.[24] Higher temperatures increase F solubility, the volatility of LiF above its melting point (848°C) inhibits fluorination of the DRX phase.[24] Based on these findings, metastable synthesis techniques are suggested for future work on DRX fluorination.[24]

Other potential methods include adopting the high-entropy alloys of multi-TM SRO[12] and Cl incorporation. For example, substitution of Cl in $Li_{1.225}Ti_{0.45}Mn_{0.325}O_2$ (LTMO) was used to form $Li_{1.225}Ti_{0.45}Mn_{0.325}O_{1.9}Cl_{0.1}$ (LTMOCl), and experimental results showed better performance for LTMOCl compared with LTMO.[25] Cyclic voltammetry (CV) results showed the potential difference of the Mn^{3+}/Mn^{4+} redox couple for LTMOCl was reduced compared to LTMO, indicating Cl substitution reduces electrode polarization.[25–27] Electrochemical impedance spectroscopy (EIS) measurements showed the low-frequency linear slope for the LTMOCl electrode was greater than that of the LTMO electrode, indicating a higher Li diffusion rate for LTMOCl.[25] **Figure 5** shows that Li diffuses via the o-t-o path, the diffusion barrier is influenced by the height (or size) of the intermediate tetrahedron. The larger ionic radius of Cl leads to an increased height of the intermediate tetrahedron in LTMOCl, thus reducing the energy barrier.[25] However, theoretical research in Cl substitution is less extensive than that in F substitution, the mechanism of how Cl influences Li migration may be materials-dependent and is not fully understood yet.

Measuring and visualizing SRO in the crystal structures can be challenging and typically requires advanced characterization techniques. Solid-state NMR (ssNMR) results suggested that the formation of the detrimental γ-$LiFeO_2$ type SRO can be explained by the local electroneutrality preference,[28] whereby each O^{2-} is coordinated octahedrally by six cations with a combined charge of 12^+. Taking $Li_{1.25}Nb_{0.25}Mn_{0.5}O_2$ as an example, the available metal cations have charges of 1^+, 3^+, or 5^+ (Li, Mn, and Nb,

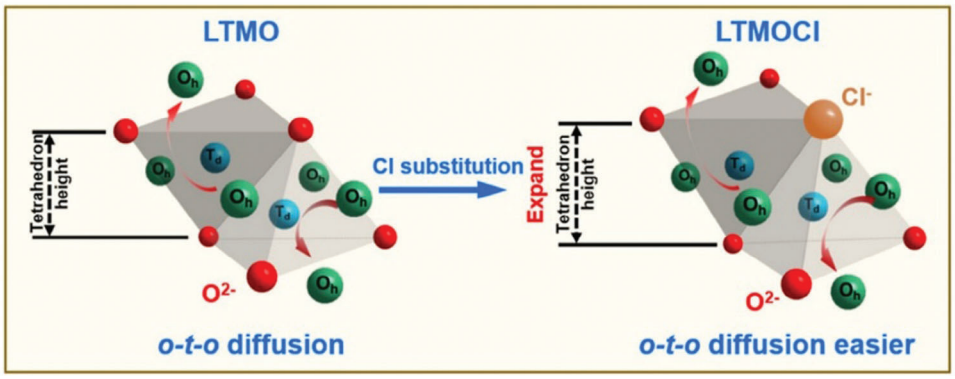

Figure 5. Schematic illustration of the local environment for Li migration in LTMO and LTMOCl. Adapted with permission.[25] 2023, American Chemical Society.

respectively), and local electroneutrality can only be achieved through the OLi_3Mn_3 (similar to γ-$LiFeO_2$) or OLi_4NbMn arrangements. The latter arrangement is better suited to the composition, with excess Mn^{3+} ions accommodated through the former arrangement.[28] Both experimental and simulations results show that both ionic charge and size influence the stability of the DRX materials. On one hand, the high-valent TMs tend to repel each other and intimately mix with Li to keep local electroneutrality, thereby inhibiting Li segregation into Li_4 tetrahedra; on the other hand, the size mismatch between high-valent TMs and Li facilitates Li segregation to minimize strain, counteracting the charge effect.[15] For trivalent redox-active TMs where the average valence of the TMs is fixed and so is the electrostatic interaction strength between Li and TMs, the size effect becomes dominant, e.g. ions with large ionic sizes such as Sc^{3+} (0.745 Å) and In^{3+} (0.80 Å) are likely to impede Li^+ diffusion, whereas other ions with smaller ionic sizes such as Ga^{3+} (0.62 Å) and Sb^{5+} (0.60 Å) are likely to facilitate Li^+ efficient transport.[15]

2.2. Materials Degradation

During the charge and discharge process of DRX cathodes, two types of redox reactions occur, namely the cationic and anionic redox, both contribute to the overall charge/discharge capacities.[29] The cathode degradation is primarily governed by: (i) TM ion migration and (ii) oxygen evolution. The dynamic behavior of TM ions during cycling which includes their continuous migration, reduction, and dissolution lead to oxygen redox, especially the release of oxygen, and changes in the electronic and crystalline structure.[29] Another significant factor contributing to the cathode degradation is the oxidative decomposition of the carbonate solvent(s) in the electrolytes at high voltages that generates water and other protic species.[30] In the standard $LiPF_6$-based electrolytes, they decompose the PF_6^- into PF_5 and HF, with further reactions lead to the formation of Lewis acidic OPF_3 and fluorophosphate salts such as $PO_2F_2^-$.[31] The TM dissolution from the cathode materials has been reported to coincide with electrolyte oxidation, rationalized by the HF formation and acid-mediated dissolution.[32] The dissolved TMs migrate through the electrolyte and subsequently to the anode where they deposit. This has been proposed to cause continuous decomposition of the solid electrolyte interphase (SEI) and electrolyte, increasing impedance.[33,34]

For the current collector of the cathode, the electrochemical stability of Al stems from the presence of a thin (≈5–20 nm) nonporous native protective layer that consists mostly of Al_2O_3 and traces of $Al(OH)_3$.[35] This layer provides high corrosion-resistance to the current collector up to ≈3.8 V versus Li/Li^+ in conventionally used organic battery electrolytes,[35–38] and the oxide film becomes susceptible to decomposition when this potential limit is exceeded or in contact with chemically aggressive electrolyte.[36,37,39,40] The electrochemical corrosion requires a contact of the metallic surface with an electrolyte solution, this may emerge due to inhomogeneity of the material and its environment, e.g. presence of impurities, grain boundaries, crystal planes, lattice defects and concentration gradient of a constituent in the solid phase.[41]

For oxygen evolution, DFT is used to calculate density of states (DOS) and charge/spin density around oxygen ions in various local environments and suggests O oxidation occurs preferably along the Li–O–Li configuration, with orphaned hole states on O^{2-}.[42] Delocalized electron-hole states over time can condense to form molecular O_2 which is either trapped within the lattice or form O_2 gas that escapes from the lattice, leading to oxygen loss.[43] Ultimately, O-redox cathodes that form hole states on O in lattice that lead to oxidized oxygen in lattice and do not transform into O_2 are desirable to deliver reversible bulk oxygen oxidation and are reversible cathode materials.[43] Using transmission electron microscopy (TEM) and neutron diffraction, peroxo-like O_2^{n-} species with long O–O bonds are visualized,[44,45] while the DFT calculation predicts the formation of peroxides O_2^{2-} as an intermediate of the anionic redox.[46,47] The contribution to energy storage by other TM and O in DRX materials is shown by combined in situ XRD and electron energy loss spectroscopy (EELS) measurements.[10]

The layer densification phenomenon[48] is one of the theories rationalizing the possible oxygen loss mechanism. Upon cycling, the observed TM-enrichment (reduction of Li-excess) leads to poorer 0-TM percolation on the particle surface, causing capacity fading and hysteresis. After the first charge, oxygen vacancies are generated on the surface, causing instability of high-valent TM cations, which are then reduced to a lower oxidation state.[49] The reduced cations may then migrate into the neighboring octahedral vacancy sites left by Li, resulting in a densified surface layer with fewer Li vacancies and lower TM oxidation states compared to that in the bulk.[49] After extensive cycling, the above densification-based degradation will be gradually extended into the bulk materials, causing capacity fading, the O_2 loss mechanism is also supported by the resonant inelastic X-ray scattering (RIXS) and NMR results[29] (details in Section 5.1.2), and neutron pair distribution function (PDF)[50] (details in Section 5.2.2).

A novel methodology for calculating the surface energy of DRX materials was developed.[51] Results from a previous cluster expansion model, trained using ab initio calculations as described,[18] are used as a basis for MC simulations to describe and equilibrate the disordered bulk structures. A robust ab initio calculation of surface energies for facets of the DRX material Li_2MnO_2F as a function of surface cation and anion decoration was performed.[51] The obtained energies were Boltzmann-weighted to obtain an average energy for each facet which were then used to calculate the equilibrium particle shape.[51] Li_2MnO_2F displays predominantly [100] type Li/F-rich facets, favoring a cubic particle shape.[51] A statistical analysis and subsequent linear regression indicated that stable surfaces were likely enriched Li and F which correlate with improved cycle life and Mn and O retention.[51]

An unusual δ phase transformation was discovered from disordered Li- and Mn-rich rock salts to a new δ phase which displays a partial spinel-like ordering with short coherence length and exhibits high energy density and rate capability.[52] Unlike other Mn-based cathodes, the δ phase exhibits almost no voltage fade upon cycling. The driving force and kinetics of this in situ cathode formation where immobile TMs, such as Ti^{4+}, play an important role in regulating the driving force for the

transformation and controlling the structure of the δ phase.[52] Design guidelines were established for Li- and Mn-rich compositions that combine high energy, high rate capability, and good cyclability, thereby enabling Mn-based energy storage, future improvements may be possible by reducing the immobile cation content to increase the length of the 4-V plateau and by replacing Mn with a multi-electron redox center to increase the theoretical TM redox capacity.[52]

The design space of compositional complex energy materials (CCEMs) is intricate due to higher dimensionality of compositional space, as well as convoluted interplay between long range order and short-range structures.[53] Progress of machine learning algorithms, the physical interpretation, and their potential applications in studying CCEMs has been reviewed.[53] To give a specific example, a machine-learning approach that predicts synthesis conditions using large solid-state synthesis data sets text-mined from scientific journal articles was developed.[54] Using feature importance ranking analysis, the optimal heating temperatures were discovered to have strong correlations with the stability of precursor materials quantified using melting points and formation energies (ΔG_f, ΔH_f).[54] This correlation between optimal solid-state heating temperature and precursor stability extends Tamman's rule from intermetallics to oxide systems, suggesting the importance of reaction kinetics in determining synthesis conditions.[54] On the other hand, heating times are shown to be strongly correlated with the chosen experimental procedures and instrument setups.[54] Using these predictive features, the authors constructed machine-learning models with good performance and general applicability to predict the conditions required to synthesize diverse chemical systems.[54]

3. Characterization Techniques to Address the Li Percolation-Based Challenges

Characterization techniques that are sensitive to Li include atom probe tomography (APT)[55] and ^{7}Li solid-state nuclear magnetic resonance (ssNMR) spectroscopy that allows the investigation of local environments of Li.[56] Other techniques that are used for studying Li percolation (sometimes include using focused ion beam, FIB, and ion etching depth profile to section the sample particles first) include neutron PDF (nPDF) for assessing the SRO structure in DRX materials;[57] X-ray absorption near-edge structure (XANES) analyzes the variations in the oxidation state of TM during Li intercalation and de-intercalation to measure the amount of Li in the material;[58] X-ray Compton scattering (XCS) that measures Li chemical stoichiometry of the electrode materials through the electron momentum ratios between the valence and core electrodes of the electrode material compounds;[59] and atomic-resolution high-angle annular dark-field scanning transmission electron microscopy (HAADF-STEM) imaging to image the atomic arrangement as the intensity recorded is proportional to the square of the atomic number Z.[60] The combined technique of HAADF-STEM with electron ptychography offers the advantage of the possibility of direct imaging of Li ions,[61] where Li and O atoms are visible in the phase image.[61] Details are shown below.

3.1. Scanning Transmission Electron Microscopy (STEM)-Based Characterization for Analysis of Li and Other Cation SRO

STEM with atomic resolution Z-contrast imaging and electron energy-loss spectroscopy (EELS) has been applied for imaging and quantifying the atomic and electronic structures of the DRX materials.[62] SRO represents a systematic local bonding preference between certain ion species. The form of cation SRO is important since the (local) structure type and the degree of (dis)order affect both Li mobility and Li percolation.[9]

High-resolution bright field transmission electron microscopy (BF-TEM) techniques are useful for uncovering the atomic arrangement characteristic of cathode materials,[63] though it is challenging to directly image the different TM atoms with similar atomic mass in the SRO.[64–66] Atomic-resolution HAADF-STEM imaging technique is complementary BF-TEM as it helps visualize the local structure, in which the image intensity recorded in HAADF-STEM mode correlates to the average atomic number Z along the atomic column and roughly proportional to Z^2. In the case of $Li_{1.3}Nb_{0.3}Mn_{0.4}O_2$, [001], HAADF-STEM images reveal variations in intensity profile for the different atomic columns.[60] Brighter atomic columns, corresponding to the peaks with higher intensity in the profile, are enriched with heavier Nb atoms, while the less intensive columns are enriched with Mn.

Nevertheless, STEM probes only a small region of the crystal and cannot represent the overall information from the whole particle. Addressing these challenges not only requires experimental techniques but also analytical approaches to determine realistic atomic-scale models of SRO consistent with experiments. One methodology is cluster-expansion MC simulation which couples first-principles energy calculations of candidate SRO models with large-scale atomistic simulations.[67] A new methodology has been developed that combines MC simulations and PDF calculations to evaluate SRO in DRX materials[68] where MC simulations allow for the construction of an $A_{1+x}B_{1-x}O_2$ phase space across a range of stoichiometries, the structures in the phase space constitute a library of calculated PDFs, each pointing to a specific cation SRO motif. Using these motifs as structure identifiers, SRO is analyzed by reverse mapping their structures via the PDFs onto the phase space.[68]

3.2. X-Ray Absorption Spectroscopy (XAS) for Analysis of Li Intercalation and De-intercalation and Oxidation State Changes of Transition Metals

XAS includes a diverse family of spectroscopic techniques, such as XANES[69] and extended X-ray absorption fine structure (EXAFS).[70] Resonant inelastic X-ray scattering (RIXS)[71] is a combination of XAS and X-ray Emission Spectroscopy (XES), where a core electron is also excited by an incident X-ray photon and this excited state decays by emitting an X-ray photon to fill the core hole in XES. The XES high-resolution fluorescence detection technique measures the X-ray absorption spectrum via monitoring the intensity of a fluorescence line corresponding to a specific excited state decay process using a narrow energy resolution, making it possible to overcome some of the main limitations of conventional XAS.[72] While XANES encompasses an energy range of 50–100 eV in close proximity to the absorption

edge, EXAFS covers a broader energy range, spanning several hundred eVs and commencing ≈30 eV beyond the absorption edge.[73] XANES analysis facilitates the determination of oxidation states and local symmetry changes of the specific absorbing element, while EXAFS provides quantitative information about the local atomic structure.[74] Synchrotron XAS is adopted for investigating both the sublattice structure and redox reactions in DRX materials, e.g. the oxyfluoride type DRX with a more sophisticated anionic sublattice.[75] This technique enables the simultaneous probing of local structure and chemical states with element-selectivity as the high intensity of synchrotron X-rays enables the detection of elements at extremely low concentrations to an extent.[76]

As for cationic sublattice studies, the variations in the bulk oxidation state of TM in pristine and cycled samples can be assessed by analyzing the reflection energy of the XANES in TM K-edge, M-edge, and L-edge. XANES examine the unoccupied density of states and the measurements are sensitive to the local bonding environment, such as the number of valence electrons, their spin configurations, and the symmetry and coordination number of the TM compound structural unit cell. Upon oxidation/reduction, the peak is expected to shift to a higher/lower energy region; the energy position corresponding to the first derivative of the rising edge is commonly used as an index of the oxidation state.[19] Alterations in the in situ XANES profile shape can be compared subsequently to the one after cycling, which signify the modifications in the oxidation states and electronic configurations of the TM. On the study of Ti-doped $LiFePO_4$ cathode ($LiTi_{0.01}Fe_{0.99}PO_4$), alternations in the Fe valence during Li intercalation and de-intercalation were observed by the in situ Fe K-edge XANES measurements,[77] indicating the role of Fe ion as electron donor/acceptor during charge/discharge.

To probe the anionic sublattice in F-DRX, F K-edge, and O K-edge spectra have been collected on various pristine samples.[78,79] A typical F K-edge XAS spectrum is comprised of three main regions: the pre-edge, absorption edge, and post-edge. These correspond to the transitions from the F_{1s} orbital to higher energy electronic states, such as TM_{3d}, F_{2p}, and F_{4s4p}. Ex situ F K-edge XAS was obtained for both the pristine and discharged $Li_{1.2}Ti_{0.2}Mn_{0.6}O_{1.8}F_{0.2}$ (LTMOF2.0) cathodes after 50 cycles with a probe depth of ≈5 nm.[79] The XAS profile exhibited sharper peaks and a newly emerging broad feature in the range of 710–730 eV, demonstrating the presence of LiF.[79] The results suggested cycling promoted the ionic character of F on the cathode surface, leading to atomic-level changes in both TM cationic sublattice and O/F anionic sublattice, as well as gradual formation and extension of domains resembling LiF on the sample surface.[79]

3.3. X-Ray and Neutron Scattering and Pair Distribution Function (PDF) for Analysis of Li SRO

Diffraction is a form of elastic scattering where the diffracted X-ray photons and neutrons have similar energy as the incident photons and neutrons. Diffraction takes place in which the uniform spacing of crystal structure causes an interference pattern of the waves present in an incident beam of X-rays and neutrons. The X-ray and neutron diffraction give complementary information. X-rays interact primarily with the electron cloud surrounding each atom, so the contribution to the diffracted X-ray intensity is larger for atoms with a large atomic number Z than it is for atoms with a small Z.[80] On the other hand, neutrons interact with the nucleus of the atoms, and the contribution to the diffracted intensity is different for each isotope, it is often the case that low Z atoms contribute strongly to the diffracted intensity even in the presence of large Z atoms.[81]

In recent years, neutron pair distribution function (nPDF) has become an increasingly popular method for probing the atomic-level structure of disordered materials.[82] The nPDF method employs neutron scattering data to study materials structures at the atomic scale, generating functions that describe the probability of locating two atoms at a particular separation distance within the material.[83] In addition to its utility in investigating the nature of O-containing species generated during cathode degradation and the coordination around O in the local structure, the nPDF technique can also analyze the SRO present in crystalline materials.

The PDF method is sensitive to the chemical properties of the SRO materials[84,85] by measuring the intensity of high-energy X-rays, neutrons, or electrons scattered from a sample at various angles.[86] PDF analysis makes use of the entire spectrum, including both Bragg and diffuse scattering. The inspection of the diffuse scattering can provide information regarding the local structure.[87] In contrast to the refinement of structures based on conventional diffraction data where only primitive unit cells are typically considered, modeling PDF data often requires the use of large supercells to account for the wide range of coordination environments that may exist.[88]

A recent study[89] performed a combination of neutron scattering and first principles simulations techniques to model SRO in $Li_{1.3}Mn_{0.4}Ti_{0.3}O_{1.7}F_{0.3}$ (LMTOF). A variety of first principles simulations techniques were used and tested, and the accuracy of each method was validated from PDF collected using total neutron scattering (**Figure 6**).[89] The PDF contained several asymmetric and bimodal peaks at short distances which arise from changes in bond lengths associated with distinct local coordination environments, referred to as displacive SRO.[89] To fully reproduce the experimental data, configurational SRO was also considered as it sets the local coordination environment of each species.[89] The results showed coupling between configurational and displacive SRO gave the best agreement with the experimental data, showing by combining these first-principles techniques with PDF analysis can be a powerful tool to provide a quantitative description of SRO.[89]

Neutron diffraction has also been applied to $Li_{1.25}Ni_{0.625}Mn_{1.125}O_3F$ to study its cubic structure and lattice parameter.[90] Sites occupied by cations were initially identified from the Fourier difference maps extracted from X-ray and neutron diffraction data, and site occupancies were then refined simultaneously against both diffraction data using a global composition restraint set to the nominal composition of this material.[90] The neutron diffraction data proved critical for correct assignment of cation occupancies on the tetrahedral 8*b* position.[90] The 8*b* site has a positive neutron scattering density overall, indicating partial occupancy with Ni that has a positive neutron scattering length compared to the negative neutron scattering lengths of ^{7}Li and Mn.[91] The local, medium, and average structures of pyrochlore $Nd_2M_2O_7$ were examined using

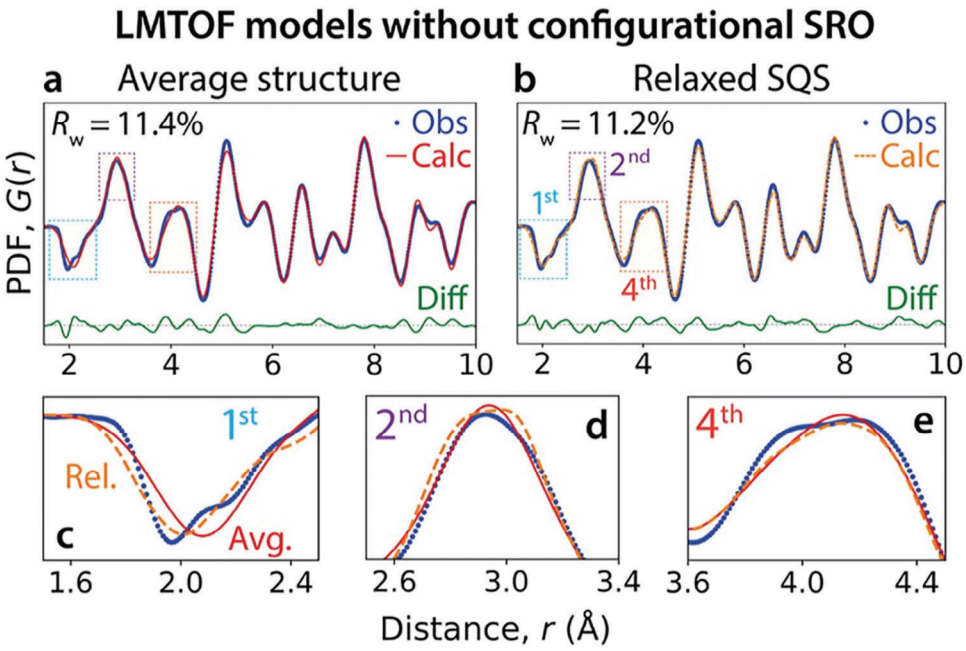

Figure 6. nPDF analysis based on random ionic configurations. a) Refinement performed using an average structure where all atoms occupy ideal positions on the fcc lattice. b) Refinement of a special quasi-random structure (SQS) relaxed with DFT calculations. Blue dots represent experimental data (Obs) and red/orange lines represent calculated values (Calc). Green lines represent the difference between these two (Diff). Panels c–e) show enlargements around the first three peaks where calculations and experiments differ most. In all cases, G(r) is plotted in terms of $Å^{-2}$. Adapted with permission.[89] 2023, American Chemical Society.

a combination of neutron diffraction and theoretical analysis method.[92] A systematic and comprehensive investigation evaluating the relationship between the local and average structure of two closely related pyrochlores was demonstrated.[92] Neutron diffraction and nPDF analysis proved that the high entropy oxides (HEOs) form as pyrochlore *Imma* structural units, local TiO_6 octahedral distortion and some degree of short-range Ti clustering were identified in the $Nd_2(Ti_{0.2}Nb_{0.2}Sn_{0.2}Hf_{0.2}Zr_{0.2})_2O_{7+x}$ compound, in contrast to the homogeneous random distribution of cations observed in $Nd_2(Ta_{0.2}Sc_{0.2}Sn_{0.2}Hf_{0.2}Zr_{0.2})_2O_7$.[92] Neutron diffraction and total scattering were also combined to investigate a series of single-phase 10-component compositionally complex fluorite-based oxides, $[(Pr_{0.375}Nd_{0.375}Yb_{0.25})_2(Ti_{0.5}Hf_{0.25}Zr_{0.25})_2O_7]_{1-x}[(DyHoErNb)O_7]_x$, denoted as $10CCFBO_xNb$.[93] A long-range order-disorder transition (ODT) at $x = 0.81\pm0.01$ from the ordered pyrochlore to disordered defect fluorite was discovered.[93] Neutron diffraction results suggested that this ODT occurs via the migration of O anions from the position 48*f* to 8*a*, with a small final jump to the ODT; however, the 8*a* O occupancy changes gradually.[93]

3.4. X-Ray Fluorescence (XRF) Scattering and X-Ray Compton Scattering (XCS) for Quantifying and Mapping Li Concentration

XRF occurs when the inner shell electrons of atoms are excited by the incident X-ray photons and subsequently release X-ray photons when the system relaxes and the electron transition from the higher energy level to the vacant inner shell.[94] The emitted secondary X-ray photons have specific energies that are fingerprints of the atoms from which the photons are originated, so XRF is used for elemental analysis.[94] XRF offers elemental detection limits in the low parts per million (ppm) range.[95] Both in situ[96] and ex situ[96–99] XRF were complemented with inductively coupled plasma (ICP) measurements for quantitative analysis of TM stoichiometric ratios in battery cathode materials.[100] In recent studies, XRF techniques are also used for characterizing F-incorporated DRX materials,[111,112,114–118] which are often unsuitable for ICP measurement due to the high ionization potential of F.[101] Total reflection X-ray fluorescence spectrometry (TXRF)[102] and wavelength dispersive X-ray fluorescence (WDXRF)[103,104] have been established for trace element analysis, their range of elemental detection has been expanded to include those with an atomic number as low as 6 (carbon).[103,104] In synchrotron XRF, elemental mapping technique is a commonly used for determining the elemental distribution and can be carried out in 2D and 3D.[105,106] As a popular cathode coating method, atomic layer deposition (ALD) of TiO_2 has been performed on the surface of various cathodes. Synchrotron XRF imaging was used to further confirm the uniformity of the TiO_2 distribution on the electrodes (**Figure 7**).[107]

X-ray Compton scattering (XCS) occurs when the outer shell electrons of atoms are ejected by the incident X-ray photons and subsequently release X-ray photons with a different wavelength as the incident X-rays in an inelastic and incoherent process.[108]

XCS is an unique technique for detecting the interactions between incident photons and valence electrons of atoms or

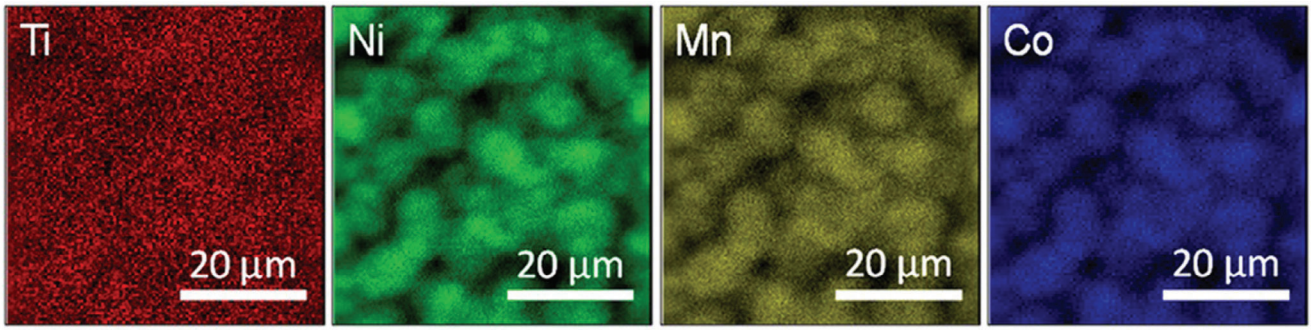

Figure 7. XRF elemental mapping of Ti, Ni, Mn, and Co for an ALD treated NMC electrode after 20 charge and discharge cycles. Adapted with permission.[107] 2019, American Chemical Society.

compounds which are involved in Li intercalation and extraction redox reactions in cathode materials.[94] A quantification method was developed to quantify changing Li stoichiometry in cathode materials (e.g., $LiNi_{0.8}Mn_{0.1}Co_{0.1}O_2$,[109,94,95] $Li_xMn_2O_4$,[110] Li_xFePO_4[111,112]) during battery cycling through calculating the electron momentum density ratio between the valence and core electrons from the X-ray scattering energy spectrum obtained by XCS. *Operando* correlative imaging of combining X-ray computed tomography (XCT)[113] with XCS imaging (XCS-I) was developed to quantify and map spatially resolved Li chemical stoichiometry distributions of the cathode compound inside different 3D electrode microstructures[114,59] to study the effects of anisotropic microstructure on Li ion diffusivity (**Figure 8**).[94,95]

3.5. Solid State Magic Angle Spinning Nuclear Magnetic Resonance (ssMAS NMR) for Directly Probing of Li Distribution and SRO

In ssNMR spectroscopy, magic-angle spinning (MAS) technique is routinely used to produce better resolution NMR spectra, MAS NMR consists in spinning the sample usually at a frequency of 1–130 kHz at the magic angle θ_m ca. 54.74° where $\cos^2\theta_m = 1/3$ with respect to the direction of the magnetic field.[115] $^{6/7}$Li NMR,[116] ^{19}F NMR,[117] and ^{17}O NMR[118] are among the most popular solid state magic angle spinning nuclear magnetic resonance (ssMAS NMR) techniques in probing the local structure and dynamics of DRX materials,[119–121,28] e.g. ^{19}F NMR is helpful for understanding the local structure of oxyfluoride-type DRX materials,[122] and ^{17}O NMR has been applied to study a range of cathode materials.[123–125,29,43,50]

^{7}Li ssNMR spectroscopy allows for the investigation of local environments of Li nuclei in both amorphous and crystalline phases.[56] Sharp ^{7}Li signals centered at ≈0 ppm correspond to Li nuclei in diamagnetic impurities, whereas the chemical shift of Li nuclei in the cathode structure is dominated by paramagnetic interactions with unpaired d electron spins of TM ions such as Mn^{3+}[126]. In DRX structures, Li ions are coordinated to 12 nearest-neighbor metal (M) ions (M = Li^+, Mn^{3+}, or Ti^{4+}) through a 90° Li-O-M bond angle and to 6 next-nearest-neighbor M ions through a 180° Li-O-M bond angle, leading to a large number of different Li environments and a broad spectrum.[126] Small ordered domains in the $Li_{1.25}Nb_{0.25}Mn_{0.5}O_2$ DRX were discovered by ^{7}Li ssMAS NMR.[28] It explained the formation of small γ-$LiFeO_2$ SRO domains within the DRX structure partially by the local electroneutrality preference, resulting in the preferential formation of OLi_3Mn_3 and OLi_4NbMn clusters for slowly cooled samples compared with rapidly cooled samples after sintering during material synthesis.[28] As the γ-$LiFeO_2$ SRO increased, there was a significant change in the probability distribution of Li nearest neighbors, leading to fewer observed resonances in the spectrum for the slowly cooled sample.[28] This in turn resulted in a greater voltage fade and poorer capacity retention as the γ-$LiFeO_2$ domains have higher Li^+ diffusion barriers.[28] Conversely, in ordered metal arrangements, such as those found in spinel or layered rocksalt oxides, the number of distinct Li environments is significantly reduced, resulting in discrete ^{7}Li ssNMR resonances.[127]

Ex-situ ^{19}F ssNMR studies on $Li_{1.15}Ni_{0.45}Ti_{0.3}Mo_{0.1}O_{1.85}F_{0.15}$ (LNF15) cathode were performed to track and analyze changes in the local F environments in the bulk and on the surface of cathode, enabling a detailed understanding of the cathode material structure.[128] Interpretation of SRO has been achieved by combining ssNMR, DFT calculations, and MC simulations (**Figure 9**).[121] It was found that the incorporation of fluorine in as-synthesized LNF15 resulted in the emergence of short-range patterns, where F atoms occupied Li-rich positions surrounded by five or six neighboring Li atoms. Furthermore, F-incorporation greatly enhanced the capacity contribution from the Ni^{2+}/Ni^{4+} pair, allowing F-bonded Ni ions to oxidize via a different mechanism, with the generated Ni^{3+} intermediate requiring lower energy to oxidize compared to those in NiO_6 octahedra.[121] Unlike in oxides, where the oxidation of Ni^{2+} to Ni^{4+} is incomplete due to the overlap between the O and Ni valence states, this outcome suggests that fluorination could be an effective approach to enhance the utilization of the Ni^{2+}/Ni^{4+} redox reservoir.[121]

In addition, ^{19}F NMR spectroscopy has also shown great potential as a powerful tool to probe the anion sites in the DRX structure.[129] However, the interpretation of the data from ^{19}F NMR can be complex due to the signal broadening arising from paramagnetic interactions between the F nuclei and neighboring open shell TM species.[69] For example: Li-Mn-Ni-O-F compounds with varying stoichiometries, the observable paramagnetic ^{19}F NMR signals were attributed to the F nuclei surrounded by six Li atoms in their first coordination shell. On the other hand, paramagnetic species, such as Mn and V, were found to be located in their second and/or third metal coordination shells.[130] However, signals originating from F directly bonded to Mn or V were

not observable due to the strong paramagnetic interactions.[130] The weak ^{19}F signal obtained for all the DRX compounds with the Li-Mn-Ni-O-F chemical space and different stoichiometries suggests that a significant fraction of F is bonded to at least one TM, consistent with the predicted behavior of the DRX materials.[130] In addition, high entropy DRX materials contain multi-cations (>3) in the structure, methods utilizing exotic nuclei, e.g. ^{61}Ni, ^{59}Co, ^{53}Cr, $^{47/49}Ti$ in NMR would be an attractive field for future studies.

3.6. Focused Ion-Beam (FIB) in Time-of-Flight Secondary Ion Mass Spectroscopy (ToF-SIMS) and Atom Probe Tomography (APT) for Analysis of Li Concentration and Diffusion

ToF-SIMS and APT can detect light elements such as Li for studying DRX materials.[131] ToF-SIMS is a surface-sensitive method that involves the ejection of secondary species from a sample outermost surface caused by the bombardment of a primary ion beam, only a small portion of the total sputtered population is ionized and can be directed toward a mass analyzer where the mass of the particles is determined by measuring the time at which they reach the detector.[132] FIB and depth profiling were used to accompany ToF-SIMS by sectioning a particle, revealing the cross-section of the particle for studying the ion distribution within the particle.[133] The ionization process is significantly influenced by the surface chemistry of the solid and surface modifications resulted from the sputtering process, commonly referred to as the matrix effect.[134] ToF-SIMS has been used to provide information on the distribution of cathode active materials when accompanied with FIB and depth profiling,[135,136] the formation of SEI during charge discharge cycles,[137–139] and detecting degradation species of cathodes.[140]

The use of an FIB scanning electron microscopy (SEM) in ToF-SIMS presents a promising approach for the detection and quantification of Li and other active elements in battery materials in both fully charged and fully discharged states, e.g. $LiNi_{0.5}Mn_{0.3}Co_{0.2}O_2$ (NMC532) down to 20 nm spatial resolution,[133,141] as the detection of discrete packets of secondary ions with varying masses as a function of time at the detector enables SIMS to exhibit the sensitivity that surpasses the analytical capability of energy dispersive spectroscopy (EDX).[142]

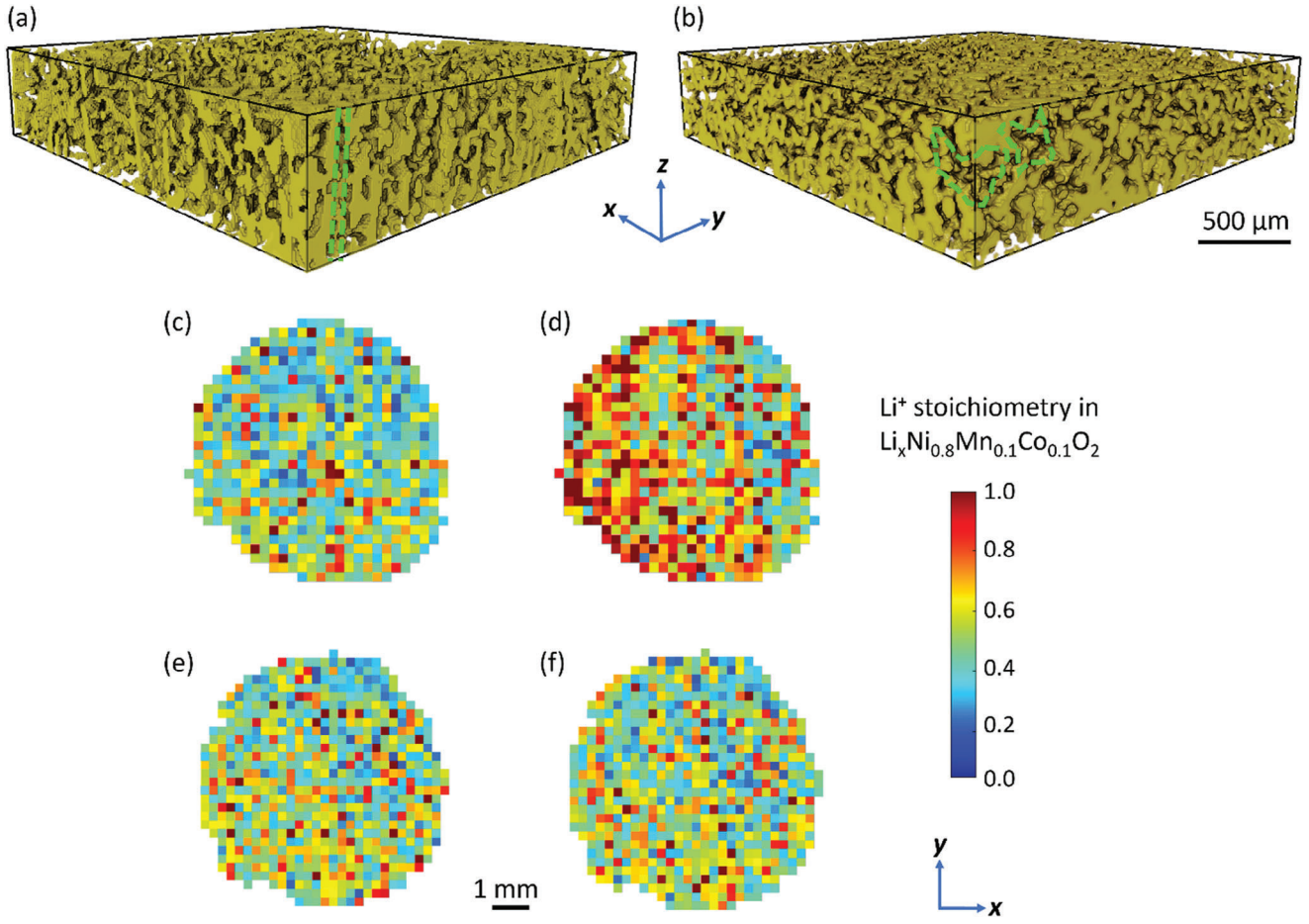

Figure 8. *Operando* correlative imaging of combining XCT with XCS-I. 3D volume rendering of a region of cathode extracted virtually from inside of an operating battery coin cell from the XCT data, showing a) vertically oriented pore arrays inside a cathode made by directional ice templating (DIT); and b) random pore orientations inside a cathode made by isotropic ice templating (IIT). XCS-I results showing voxel-by-voxel color maps of the lateral distribution of Li chemical stoichiometry in the middle depth region of the DIT cathode at c) charged to 4.3 V; d) discharged to 2.75 V; and of the IIT cathode at e) charged to 4.3 V; f) discharged to 2.75 V. Adapted with permission.[114] 2023, Elsevier.

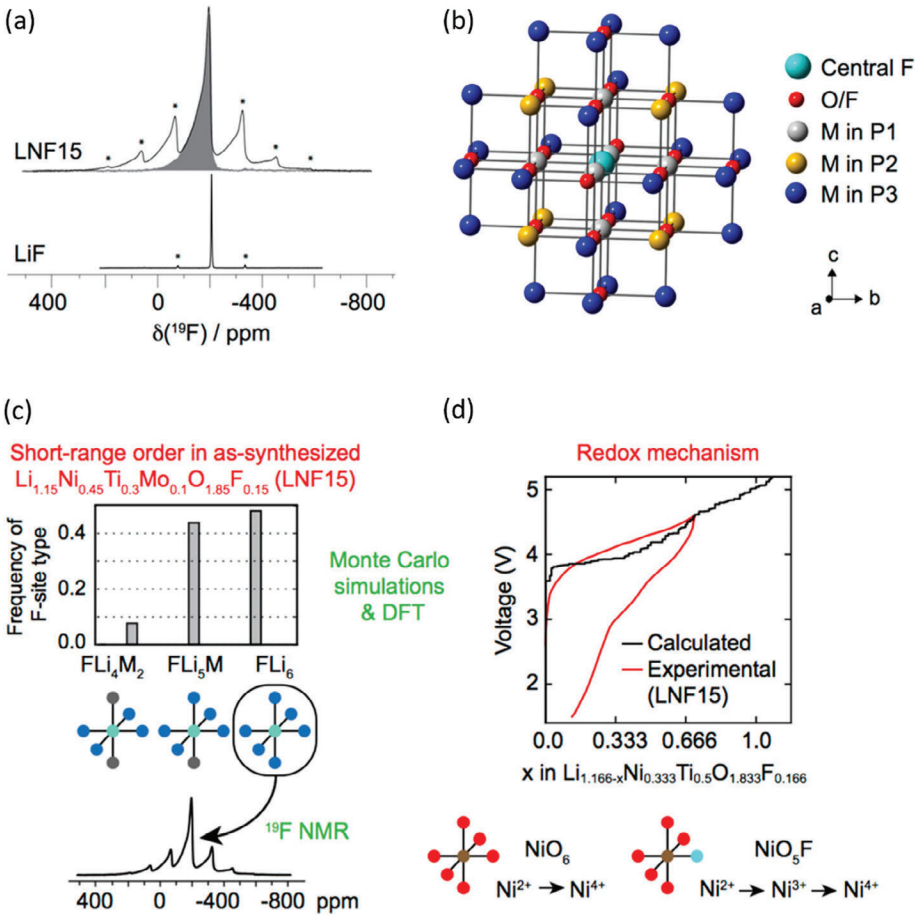

Figure 9. a) The ^{19}F spin echo NMR spectra were acquired for LNF15 and LiF powders using 60 kHz MAS. The spin echo spectra display spinning sidebands, which are marked with asterisks. The isotropic spectrum of LNF15, obtained through ^{19}F projected magic angle turning phase-adjusted sideband separation (pj-MATPASS), is depicted with a gray shading. b) The typical fluorine (F) local environment in a rocksalt TM oxyfluoride compound is illustrated, showcasing the first three coordination shells (P1, P2, and P3) surrounding the central F atom. c) SRO in as synthesized LNF15 is illustrated by the frequency of F-site types through DFT and MC simulation. The observed emergence of new signals in the ex situ ^{19}F NMR spectra at high states of charge corresponds to diamagnetic F environments seen in the computed models. d) Calculated and experimental redox mechanism suggesting that nickel ions in octahedral coordination, when bonded directly to F, undergo a distinct oxidation mechanism compared to those surrounded by six oxygens. In this case, the nickel ions form Ni^{3+} intermediates instead of transitioning directly from Ni^{2+} to Ni^{4+} during oxidation. Adapted with permission.[121] 2018, American Chemical Society.

Consequently, SIMS can detect trace quantities of low-mass elements, e.g. Li on surfaces.[143] The resulting ions or species-specific nanoscale maps revealed both crystallographic orientation and chemical effects in primary grains of the cathode material.[143] **Figure 10** shows that the Li ions became localized and exhibited constrained mobility at the interfaces between particle-matrix interfaces, as well as at grain boundaries.[141] The ^6Li and ^7Li isotopes tracer diffusion coefficients of $LiMn_2O_4$ thin films (200–300 nm thick) were determined via isotope ion-exchange and SIMS line analysis.[144] The edge effects are localized fluctuations in signal intensity, may arise due to changes in the sputtering yield caused by the sample topography, and the matrix effects arise because each material exhibits a distinct emission response to the primary ion-beam sputtering,[133] both affecting the SIMS results. Experimental calibration is required for different materials to determine their corresponding Li concentrations. Nanoscale elemental distributions of $LiMnO_2$ and other electrode materials were also reconstructed using APT,[145,146] showing the 3D distributions of elements such as Li, Mn, and O.[146] In contrast to a homogeneous distribution of Li observed in a $LiNi_{0.5}Mn_{1.5}O_4$ cathode, research revealed the existence of a heterogeneous distribution of Li in the cycled spinel $Li_{1.2}Ni_{0.2}Mn_{0.6}O_2$ cathode, indicating a pronounced loss of Li upon cycling.[147] APT provides 3D high resolution compositional mapping of elements including H, C, or Li with sub-nanometer resolutions where the surface atoms from a sample in the shape of a very sharp tip are evaporated by field effect (near 100% ionization) and the resultant ions are projected onto a position sensitive detector (PSD) that are identified by their mass-to-charge ratio using a ToF mass spectrometry.[148]

4. Characterization Techniques to Address the Materials Degradation Challenge

Characterization techniques that detect elemental mixing include HAADF-STEM that measures the changing distances of

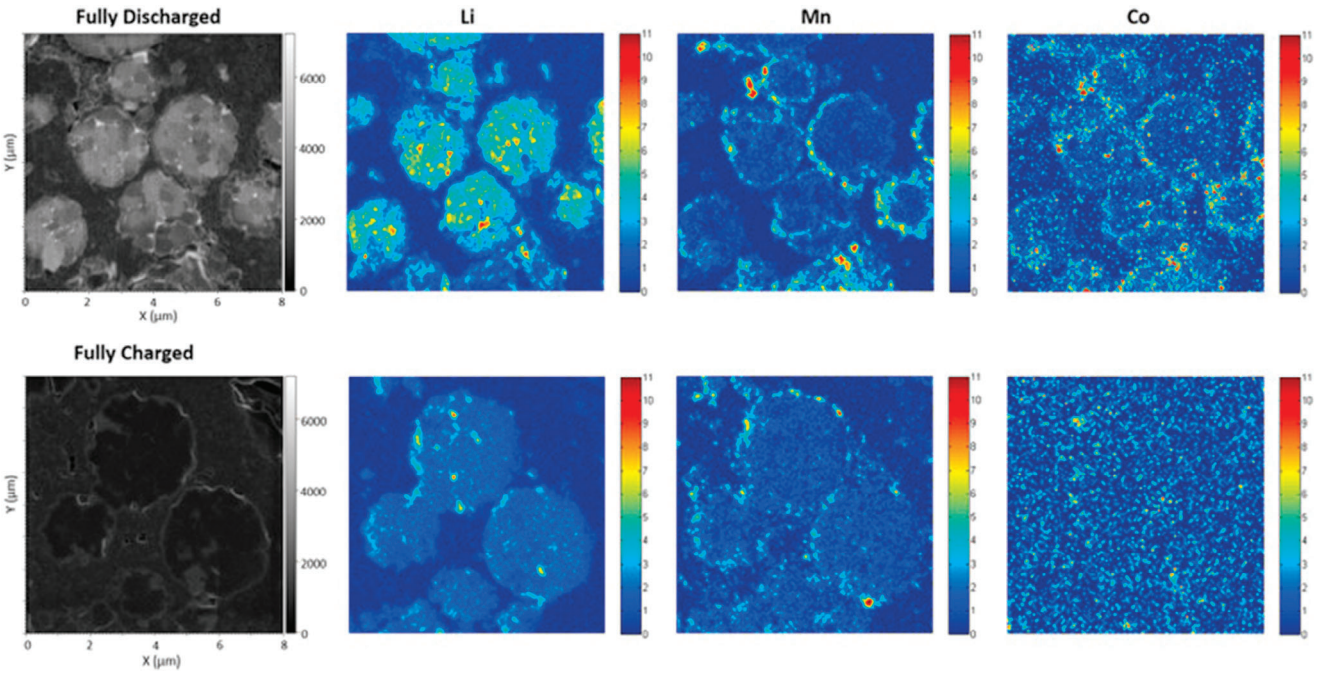

Figure 10. The mapping of FIB-SEM/ToF-SIMS, which involves the combination of secondary electron images obtained from FIB-SEM with three normalized elemental distribution maps of Li, Mn, and Co for the fully discharged (top row) and fully charged (bottom row) samples. The entire field of view measures 8 μm. Adapted with permission.[141] 2015, Elsevier.

TM-TM and O-O for resolving structural degradation of the materials through O and TM migration;[61] combining XAS and scanning transmission X-ray microscopy (STXM) that acquires nm resolution mapping of chemical species within individual particles to study dissolution mechanisms;[149] and ToF-SIMS depth profiling and high-resolution imaging[150] and APT[151] that have been used to visualize the concentration and spatial distribution of degradation species on the surface of active cathode particles.

Characterization techniques focusing on studying O loss degradation mechanism include ^{17}O ssNMR that probes local chemical environment around O,[29] and combining O-K resonant mapping of resonant inelastic X-ray scattering (RIXS), nPDF and ssNMR that identify the O redox and trapped molecular O_2 in the materials.[50] Finally, the electrochemical mass spectrometry (EC-MS) monitors the formation of intermediate species and gas evolution during electrochemical reactions to uncover unexpected side reactions.[152] We show each of the characterization techniques and their complementary use in the following section.

4.1. STEM-Based Characterization for Probing Structural Evolution and O-Redox During Cathode Degradation

HAADF-STEM imaging was used for resolving the structural degradation in bulk cathode during cycling.[21] The development of various O-redox models has been heavily debated from computational chemistry,[42,44–47] **Figure 11** shows HAADF-STEM and fast Fourier transform (FFT) demonstrated structural transformation in DRX materials is attributed to irreversible O-redox and loss of O_2 during cathode degradation processes.[21] The RIXS and NMR results explain the O_2 loss mechanism at bulk and surface levels occurs through in-plane TM migration, and F-incorporation stabilizes DRX structures by surface O_2 suppression.[29] The unified O_2 loss mechanism applies to a range of layered rocksalt materials, with the trapped molecular O_2 in the bulk level supported by evidence from the nPDF.[50] As an innovative approach to characterize the anionic redox in rocksalt cathodes, electron ptychography was applied to directly image oxygen shifts in $Li_{1.2}[Ni_{0.13}Mn_{0.54}Co_{0.13}]O_2$.[153,154,61] Oxygen shifts were seen in both the bulk and surface, which is indicative of the unified O_2-loss mechanism,[29] where solid O_2 molecules appear to be generated and trapped in the bulk during cycling.

EELS mapping can directly visualize the distribution of Mn oxidation states near the surface. **Figure 12** shows the reduction of the Mn valence can be reflected by the shift of the Mn L3 peak to lower energies in EELS mapping. A uniform elemental distribution in the pristine particle was observed, and formation of nanoscale voids in the cycled one, as indicated by the HAADF-STEM images and corresponding EELS maps.[155] Recent work uncovers a heterogenous $Li_{1.68}Mn_{1.60}O_{3.7}F_{0.3}$ (LMOF0.3) cathode, composed of three distinct domains of spinel-like, DRX-like, and layered-like phases, in contrast to the traditional single-phase DRX cathodes.[156] The nanocomposite material exhibited different average Mn oxidation states for the spinel and rocksalt regions, as indicated by the varying ratios of Mn-L_3/L_2 peaks observed in the EELS analysis of the two distinct regions. Ti was doped to enhance the DRX content within the spinel-like matrix of the nanocomposite particle and increased capacity retention by ≈30% after 50 cycles due to

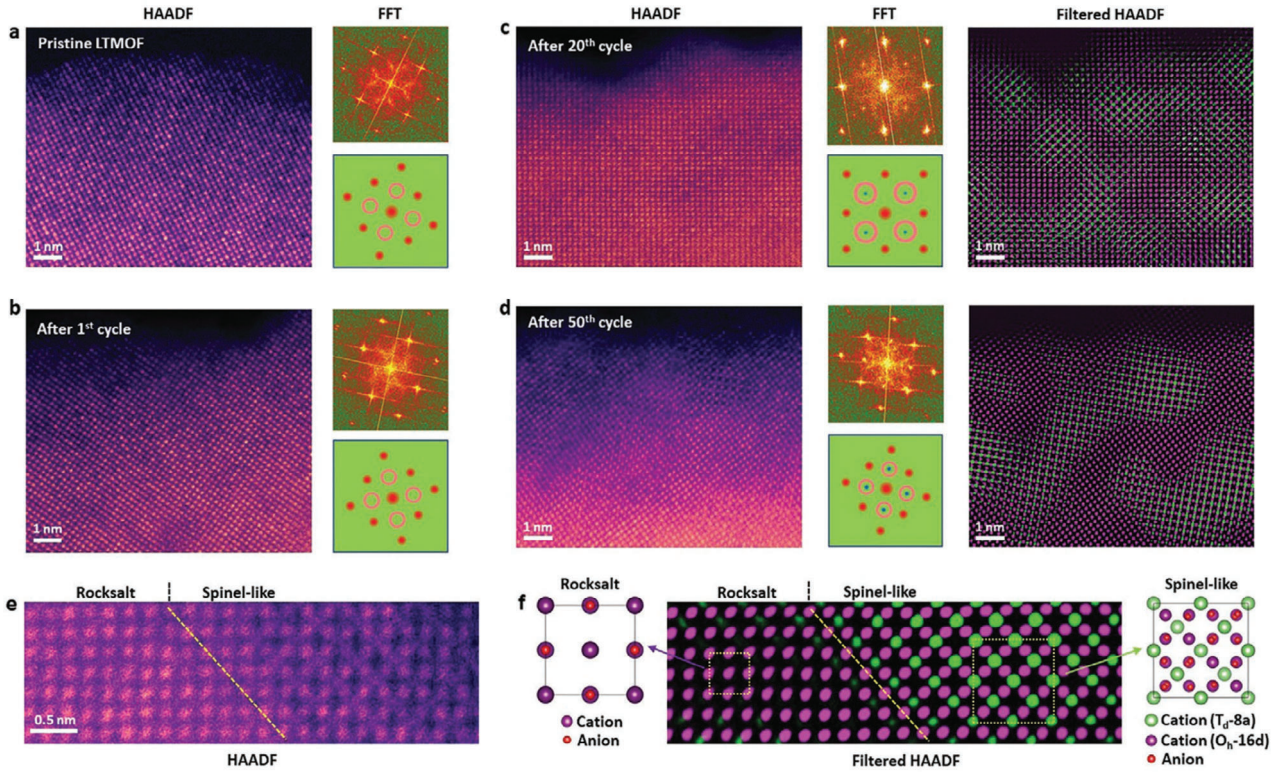

Figure 11. Degradation of $LiNi_{0.5}Ti_{0.5}Mn_{1.5}O_4$ (LTMO) and $LiNi_{0.5}Ti_{0.5}Mn_{1.5}O_4F_{0.2}$ (LTMOF) cathode materials has been studied by a combined technique of HAADF-STEM and FFT, where a rocksalt-to-spinel-like structural transformation was observed upon cycling. By filtering the structural information in the Fourier transform, a combination of the filtered images showed that the nanosized spinel-like domains were dispersed in the rocksalt matrix. Further analysis using atomic-scale HAADF-STEM imaging showed that the structural change occurs gradually and continuously upon cycling. A magnified HAADF-STEM image of a boundary between rocksalt and spinel-like regions in LTMOF after 50 cycles signifies a disordered spinel-like structure, where the Td-8a sites were occupied by both Li and TM atoms. EELS elemental maps and spectra of the mixed-phase structures in LTMOF after 20 cycles indicated that there was no elemental segregation within different phases and the TM valences were consistent across different phases at the same depth beneath the surface. Reproduced with permission.[21] 2022, John Wiley and Sons.

the reduction of cooperative Mn^{3+} Jahn-Teller distortion and O-loss.

Combining STEM with electron ptychography offers the advantage of direct imaging of Li ions, this is highly beneficial in studying cathode material degradation mechanisms in LIBs.[61] Electron ptychography can uncover the movement of both heavy and light atoms during electrochemical reactions to understand the atomic structure and calculating the projected atomic bonds of battery materials in relation to their redox mechanisms. Focused-probe electron ptychography was utilized to investigate the average projected O-O distance at various stages in the first charge-discharge cycle, revealing oxygen deformation in the lattice structure. The method was applied to obtain simultaneous HAADF and ptychographic phase images of pristine $Li_{1.2}Ni_{0.13}Mn_{0.54}Co_{0.13}O_2$ projected parallel to the layers, with Li and O atoms invisible in the HAADF but visible in the phase image, allowing for direct measurement of the projected distance (**Figure 13**).[61] The atom distance was derived from multiple measurements using line profiles, although the values can be distorted due to sample drift during the slow-speed acquisition of the 4D datasets, which are sensitive to both heavy and light elements.[157] To generate zero-drift HAADF images and obtain the zero-drift TM-TM distances, multi-frame fast scanning of the HAADF images followed by rigid and non-rigid registration were performed, which served as a reference to calibrate the values directly measured from the ptychographic phase images at each charge-discharge stage. These distances were then used as a reference to calibrate values measured from the ptychographic phase images at each charge-discharge stage, and to quantify the changes in layer spacing and distortion of O octahedra coordinating the TM species during the first cycle.[61]

High-resolution STEM imaging is susceptible to sample drift and beam damage, which are further amplified in 4D STEM due to the longer dwell time required.[158] To address these issues, a multi-frame fast acquisition approach was conducted, which fractionates the dose across several images and reduces sample damage.[61] The postprocessing of the multi-frames using rigid and non-rigid registration algorithms produced high signal-to-noise ratio and zero-drift HAADF images.[159] The TM-TM distances derived from the zero-drift HAADF images were then used to calibrate distances in the ptychographic phase image, and the difference ratio was used to calibrate the O-O distances. The changes in the statistically analyzed O-O projected distance can reveal how the O shifts and how the TMO_6

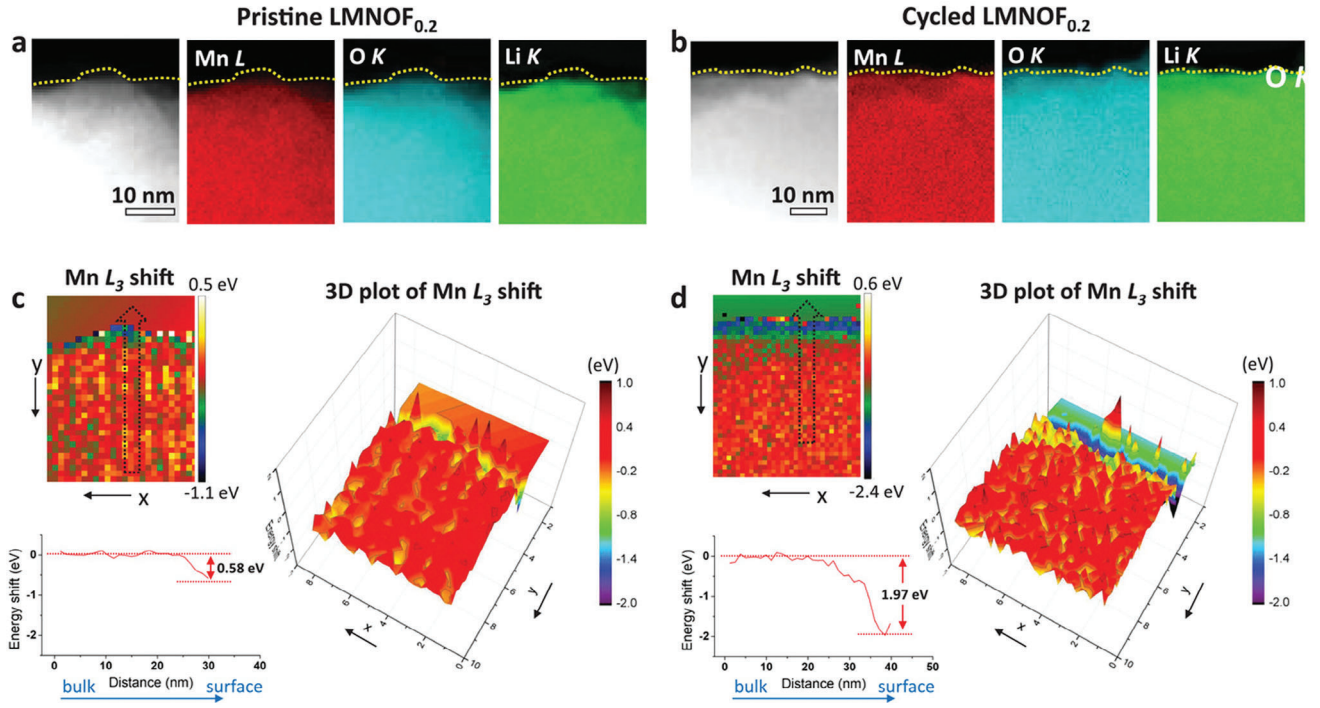

Figure 12. Cycling-induced chemical reconstruction and Mn oxidate states evolution in $Li_{1.2}Mn_{0.7}Nb_{0.1}O_{1.8}F_{0.2}$ ($LMNOF_{0.2}$) cathode particles. HAADF-STEM images and corresponding EELS maps of nanoscale surface regions in a) a pristine particle; and b) a cycled particle. Corresponding color maps of the Mn L3 peak energy shift for c) pristine; and d) cycled particles. Converted 3D surface plots on the right side. Line profiles for the energy shifts measured along the direction marked by the black dashed arrows in the 2D maps are plotted at the bottom. Reproduced with permission.[155] 2024, John Wiley and Sons.

octahedra distort at different stages of cycling in the bulk region.

4.2. Combinations of Resonant Inelastic X-Ray Scattering (RIXS), STXM, and XAS for Analysis of O-Redox

A spectroscopic study of the O K-edge was conducted to probe the electronic structure of O in the charged material following one day and one month of rest.[43] High-resolution RIXS and soft XAS were used in combination to measure the filled and empty O *2p* states of the cathode materials, respectively.[43] Previous research shows that RIXS of the O K-edge can overcome some of the limitations of conventional O K-edge XAS due to higher sensitivity to unconventional states that are triggered at very high and low voltages, making it a complementary method for detecting lattice oxygen redox.[160] Unlike the conventional O-K XAS, the oxidized oxygen in the lattice can be distinguished from the stronger and broader signals associated with TM-O hybridization in the emission energy in RIXS.[161]

RIXS is a photon emission technique, it typically offers greater bulk sensitivity compared to X-ray photoelectron spectroscopy (XPS) .[162] O RIXS maps were obtained by collecting the emission spectrum at a series of excitation energies across the O K-edge. In the one-day sample, a feature at 528 eV was evident in the XAS.[163] At this excitation energy in the RIXS map, an intense energy loss feature centered 1 eV below the elastic line was observed, there was also evidence of emission intensity at 0–1 eV energy loss, suggesting there are electronic states in this band all the way up to the Fermi level, supporting that the new O *2p* electronic states are delocalized.[43] For the charged cathode material following one month of rest, there was a decrease in the intensity of the 528 eV features in the XAS spectrum and RIXS map, and growth in intensity at 531.5 eV. The decrease of the feature at 528 eV and increase at 531.5 eV by RIXS and XAS reflect the decay of the oxidized oxide ions to trapped oxygen, partially contributing to oxygen loss.[43] The RIXS line scans reveal a broad peak at 7.5 eV and a series of sharp peaks between 0–2 eV, which indicate the formation of molecular O_2 gas through bulk oxygen oxidation and also contribute to oxygen loss.[164]

RIXS and XAS were complemented by solid-state ^{17}O MAS NMR which is a bulk average probe of the local chemical environment around O and quantifying the amount of O_2 present in the bulk.[29] Through enrichment cathode materials with NMR-active ^{17}O nuclei, a new, strongly paramagnetic chemical environment forms during O redox, and a sharp, defined sideband manifold indicated that O_2 molecules that were rigidly confined within the crystal structure.[124] Through combining ex situ RIXS and in situ nPDF, the presence of short 1.2 Å O-O distances in a positively charged O-redox cathode material were demonstrated,[50] closely matched with the bond length in molecular O_2.[165] The detection of molecular O_2 trapped in the material via nPDF provided a valuable complement to X-ray spectroscopy studies, such as RIXS.[71] They provide an initial structural proof of trapped O_2 in Li-rich cathodes. The approximate quantity of detected molecular O_2 was calculated to make up ≈20% of the O atoms

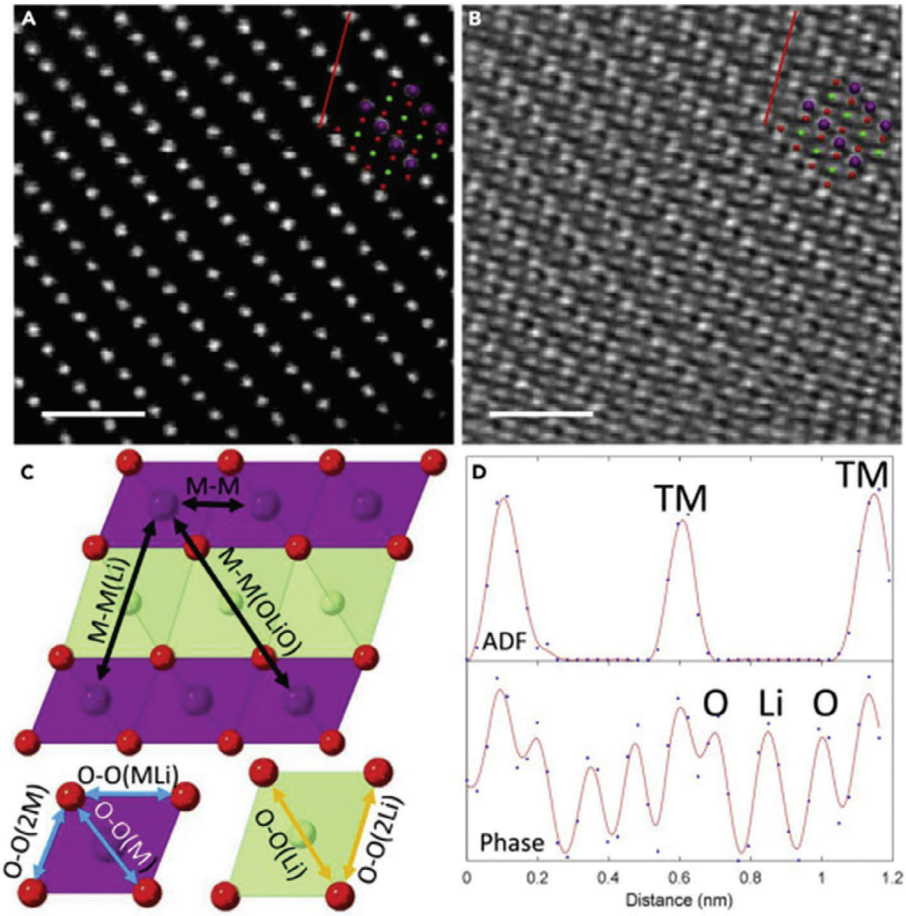

Figure 13. The measurement of the projected atom distance from [010] monoclinic zone axis of $Li_{1.2}[Ni_{0.13}Mn_{0.54}Co_{0.13}]O_2$ using A) HAADF and B) weak-beam dark-field (WDD) imaging in a 4D STEM dataset. The atomic model is superimposed, with purple representing TM, red representing O, and green representing Li. The scale bar in A and B is 1 nm. The illustration in (C) depicts the named atom distances in TMO_6 (purple) and LiO_6 (green) octahedra, with atom types in the brackets of the names indicating nearby species to the midpoint of the projected bond. D) shows line profiles across the red lines from the HAADF and WDD phase images, with the phase image pointing out the locations of Li and O where they were absent in the line profiles from the HAADF image. Adapted with permission.[61] 2022, Elsevier.

present in the cathode.[30] Integration from interdisciplinary subjects is expected to offer RIXS even more powerful applications with developing machine learning RIXS imaging techniques to achieve RIXS measurements with desired spatial resolution,[166] as machine learning is capable of handling large volumes of high-dimensional and noisy data generated by synchrotron techniques. This approach will provide unique insights into the interactions among multiple coexisting redox-active species in a range of battery cathodes, including DRX.[166]

Synchrotron-based XAS combined with STXM with high-resolution mapping at the scale of 20 nm acquired 2D quantitative data regarding the distribution of chemical species.[167] The combined STXM-XAS approach provides valuable insights into the distribution of chemical species, including their elemental composition and oxidation state.[168] Furthermore, the combination of STXM with angle-scan tomography permitted 3D microscopic analysis.[168] Spatially resolved 2D- and 3D-STXM were applied to reveal the variation of charge heterogeneity and cationic redox pattern in the DRX material $Li_{1.3}Mn_{0.4}Nb_{0.3}O_2$[169] and high-nickel, low-cobalt NMC.[149] 3D full field transmission X-ray microscopy (TXM) technique permits a quantitative evaluation of the 3D charge distribution, accounting for 20 million of XAS data (with $\approx 30 \times 30 \times 30\ nm^3$ nano-domain resolution) (**Figure 14**).[149] The depth-dependent analysis indicated that the surface of the material was highly oxidized, which can be attributed to the presence of a core-shell charge distribution.[149] Ex situ analysis with STXM-XAS was conducted on a phosphine-modified $Li_{1.17}Mn_{0.44}Ni_{0.35}Co_{0.04}O_2$ cathode that revealed the presence of a distinct area with high O, F, and C content between the secondary particles due to the agglomeration of the binder and conductive carbon where the low atomic mass of the associated elements are usually challenging to be detected and visualized using conventional electron microscopy techniques.[170]

4.3. ssMAS NMR for Analyzing O-Redox

^{17}O ssMAS NMR can probe the local chemical environment around O in a bulk average manner, which has the potential for quantifying the amount of O_2 present in the bulk and

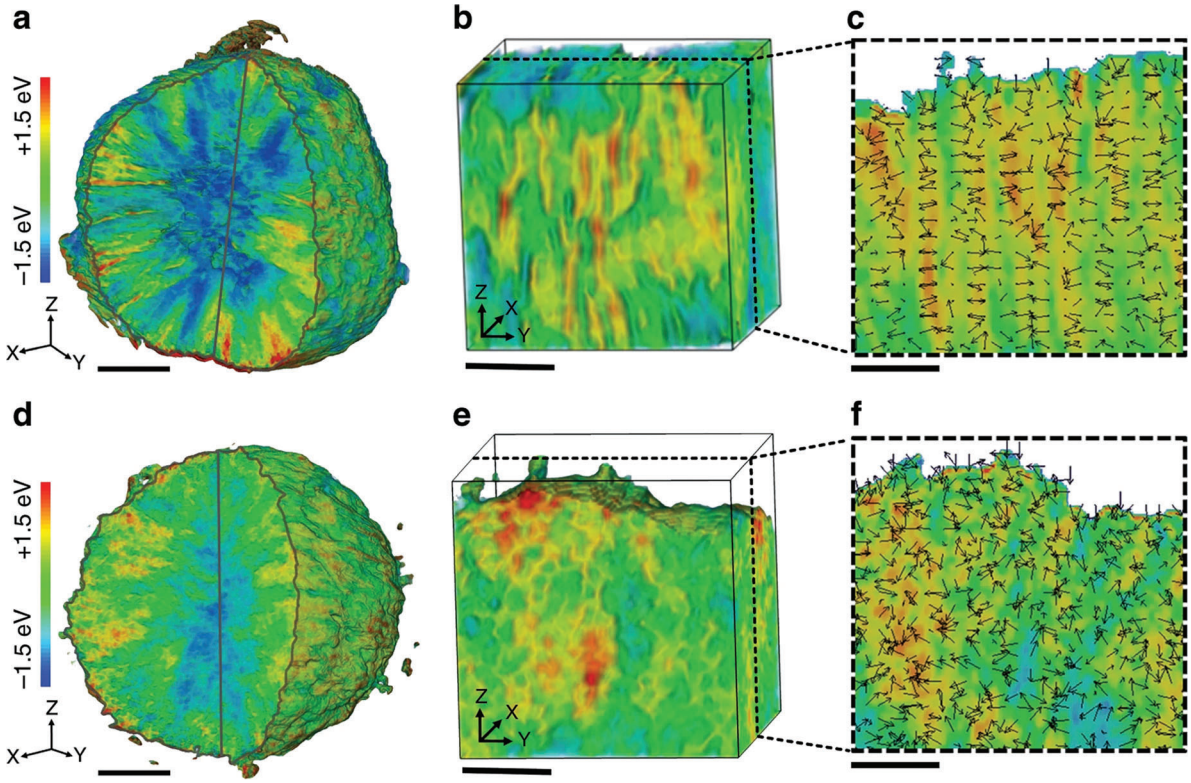

Figure 14. 3D TXM results illustrate the distribution and dimension of the high valence Ni domains. a) Distribution of Ni valence states in three dimensions; b) Representative area displaying the distribution of Ni valence states in three dimensions; c) Valence gradient of nanodomains in a 2D plane for rod-shaped NMC (Nickel Manganese Cobalt); d) 3D distribution of Ni valence states; e) Representative region depicting the 3D distribution of Ni valence states; f) 2D valence gradient of nanodomains for gravel-shaped NMC. The nanodomain valence gradient vectors are illustrated by black arrows, with the direction and magnitude of the vector represented by the arrow's orientation and length respectively. The scale bars in (a) and (d) measure 3 µm, while the scale bars in (b–c) and (e–f) measure 1 µm. The color scheme for the Ni K-edge absorption energies is as follows: blue corresponds to lower edge energy, while red indicates higher edge energy. Adapted fwith permission.[149] 2020, Springer Nature.

understanding the anion redox mechanism to utilize the extra capacity from O-redox in DRX while suppressing the irreversible O_2 loss. The unified O-redox model[123–125,29,43,50] with the trapped molecular O_2 is a result of combined STEM, RIXS, nPDF, and ssNMR analysis, where ^{17}O NMR indicates that the molecules are physically trapped in a condensed, solid-like environment. In another study, the nature of the hole states on O^{2-} before the formation of molecular O_2 and the chemical environment around the oxide ions in $Na_{0.6}[Li_{0.2}Mn_{0.8}]O_2$ were probed using ^{17}O ss-MAS NMR with ^{17}O-labelled samples.[43] The pristine material showed two well-defined chemical environments attributed to oxide ions bonded to two Mn (O-Mn_2) and three Mn ions (O-Mn_3).[43] Fast-relaxation ^{17}O ssMAS NMR revealed the existence of a strongly paramagnetic chemical environment of O for the charged material, which increased in intensity over time, further proved the presence of molecular O_2 trapped within the bulk of the cathode.[43]

4.4. ToF-SIMS and APT for Detecting Degradation-Induced Species in Cathodes

Extensive cycling of cathode materials is known to result in structural degradation such as amorphization and void formation at the surfaces of particles, which impede Li transport and cause rapid capacity loss.[21] However, highly fluorinated DRX cathodes exhibit much less prominent cycling-induced surface degradation, leading to greatly improved cycling stability.[19–21] Previous research suggests that the chemical and structural stability near the surface of cathode materials is critical in determining cycling performance.[171,172] A comprehensive understanding of the cycling-induced chemical reconstruction and TM oxidation states evolution associated with the structural evolution near the surface of cathode materials remained limited, e.g. the effects of fluorination on the cathode electrolyte interphase (CEI) layer formation on the surface of cathode particles remain unclear. This requires characterization such as using ToF-SIMS which was used in the study of cycled DRX cathodes, $Li_{1.2}Mn_{0.4}Ti_{0.4}O_2$ (LMTO), and observed the existence of a thick and unstable CEI layer on cycled particles due to surface oxidation and dissolution of TMs (Mn^{3+}, Mn^{4+}), loss of CO_2 and O_2, and crystal structural changes.[173]

ToF-SIMS depth profiling and high-resolution imaging were used to study degradation of Ni-rich layered TM oxide cathodes and spinel cathodes, e.g. $NaNi_{0.7}Mn_{0.15}Co_{0.15}O_2$ (NMC701515)[150] and TiO_2-coated Ni-rich layered cathode,[174] to visualize and monitor the concentration and spatial distribution

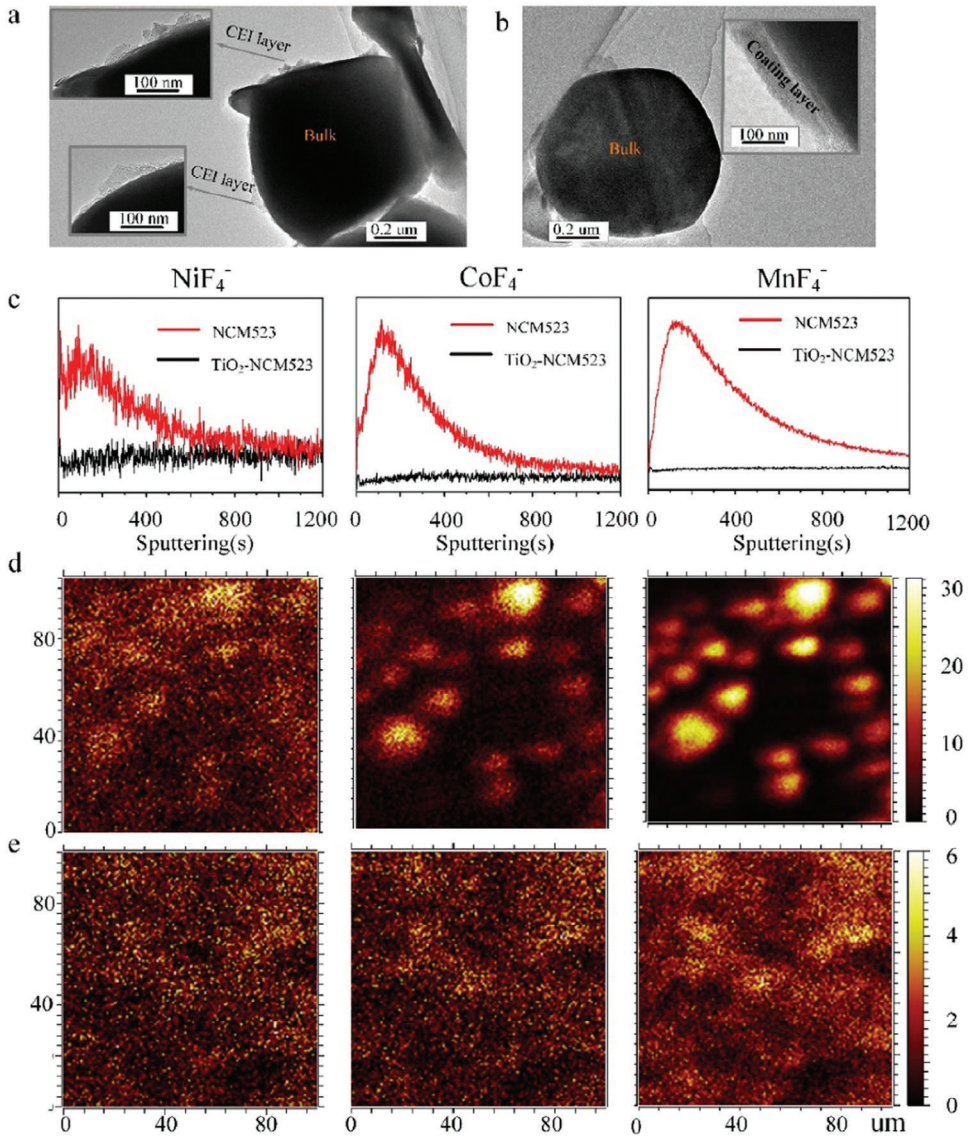

Figure 15. Transmission electron microscopy (TEM) images of two cathodes, NMC523 and TiO_2-NMC523, after undergoing 200 cycles within a voltage range of 2.7–4.5 V. a) shows the TEM image of the NMC523 cathode, while b) shows the TEM image of the TiO_2-NMC523 cathode. The figure also includes depth profiles of NiF_4^-, CoF_4^-, and MnF_4^- collected on the NMC523 and TiO_2-NMC523 cathodes in (c). Illustrative ToF-SIMS chemical mapping is presented in (d) and (e) for the NMC523 and TiO_2-NMC523 cathodes, respectively, after 200 cycles. Adapted with permission.[174] 2020, Elsevier.

of degradation species on the surface of active cathode particles, including adsorbed species, identified as $C_3H_2^-$, sodium residues, identified as $NaC_2O_2^-$, and nickel oxide, identified as $^{62}NiO^-$ for NMC701515[150] and NiF_4, CoF_4, and MnF_4 for the TiO_2-coated Ni-rich layered cathode (**Figure 15**).[174] The signal strength of the TM species was relatively lower for the coated sample owing to the effective TiO_2 coating. A significant accumulation of F^- was found on the cathode surface and deeply into the bulk particles, indicating pronounced chemical reactions between the NMC701515 particles and the polyvinylidene fluoride (PVDF) binder in the cathode.[150] CEI on two LMNO spinel cathodes, $LiMn_{1.5}Ni_{0.5}O_4$ and $Li_{1.2}Mn_{0.6}Ni_{0.2}O_2$, and an ultra-low cobalt cathode content material, $LiN_{i0.94}Co_{0.06}O_2$, were studied using ToF-SIMS, showing all the three cathode materials were initially covered by carbonate and hydroxyl-based CEI that underwent a dynamic change in chemical composition due to continuous electrolyte decomposition, particularly at high voltage.[175] Combined systematic XPS and ToF-SIMS were used to investigate Li- and Mn-rich $Li_{1.2}Mn_{0.6}Ni_{0.2}O_2$ (LMNO) cathode materials[176] and Li_6PS_5Cl-based NMC composite cathodes,[177] as TOF-SIMS has a very high sensitivity toward compounds with high ionization probabilities (several orders of magnitude compared with XPS) and can detect relative concentration changes in decomposition products.[178] The results show a non-uniform coverage of the CEI on the particles after 100 cycles.[176]

Table 1. A summary of the various techniques described above and their characteristics relevant to studying DRX materials.

Technique	Spatial resolution	Time / temporal resolution	Typical sample mass	Structural information obtained	Detection limit	Typical penetration depth	Refs.
STEM	0.4 Å–≈1 Å (aberration-corrected)	10 minutes (imaging mode, no cryogenic conditions) – 24 hours (with cryogenic conditions to stabilize the system)	100 ng – 1 µg	2D imaging of atomic arrangement	Difficulty in imaging light element atoms, e.g. Li	≈1 µm (depending on beam energy and spot size)	[63,61,186]
APT	1 Å – <1 nm (depending on metallic or more semiconducting material samples)	1.5 ns (decay line detector)	1 µg – 10 µg	3D imaging of chemical compositions and position of atoms including light elements, e.g. Li	Low data acquisition yield as some materials may not be stable in the high electric field	1 Å – 3 Å (depending on metallic or more semiconducting sample materials)	[151,180,187]
ToF-SIMS	40 nm – <100 nm, mass resolution of 10 000 atomic mass units	≈300 ns (primary ion pulse width)	100 µg – 1 mg	Elemental detection and mapping including light elements, e.g. Li, O, F High sensitivity (4 ppb) under high vacuum conditions (10^{-9} Torr)	Cannot detect the oxidation states of the elements	≈1 nm (surface sensitivity for acquiring spectra)	[133,132,135]
XANES	50 – 100 nm for spatially resolved spectra. Chemical characterization, typical spectral resolution 0.5 – 1.7 eV	100 femtoseconds – 10 minutes	5 –10 mg	Local bonding environment, e.g. number of empty valence states	Difficulty in detecting light elements, e.g. Li	10 µm-2 mm	[78,79,188,189,190]
RIXS	0.5 – 2 µm for spatially resolved spectra. Chemical characterization, typical spectral resolution 2 – 15 meV)	100 femtoseconds – 10 minutes	5 µg – 5 mg	Local bonding environment, e.g. number of filled valence states	Low count rates (requires a substantial incident photon flux)	10-200 nm (soft X-rays of ≈1 keV), 1–10 µm (hard X-rays of ≈10 keV), depending on X-ray energy	[191,43,192,189,193]
Neutron diffraction	5–10 µm for neutron imaging, neutron diffraction itself does not provide a real-space image	25 ms per frame (depending on beam intensity and detector performance)	50 mg – 1 g	Crystal structure, lattice parameter, SRO	Lower spatial resolution and slower data acquisition compared with some of the other techniques	200 µm – 100 mm (depending on materials, bulk sensitivity)	[90,92,194]

(*Continued*)

Table 1. (Continued).

Technique	Spatial resolution	Time / temporal resolution	Typical sample mass	Structural information obtained	Detection limit	Typical penetration depth	Refs.
ssNMR	Atomic spectral resolution by rapidly spinning at magic angle of 54.74° with respect to the external magnetic field, depending on the magnetic properties of samples materials	>10 µs relaxation times (depending on material, e.g. paramagnetic with rapid response or diamagnetic with slow response to applied magnetic field)	2 mg – 10 mg	Local chemical environment including light elements, e.g. Li, O, F	Lower spatial resolution compared with some of the other techniques	200 µm – 100 mm (depending on the frequency of electromagnetic wave and electrical conductivity of materials, bulk sensitivity)	[115, 116, 195]
XCS	10 µm – 200 µm in the mode of acquiring energy spectra, depending on the pixel size of the detector	10 seconds – 20 minutes (depending on operating frequency of the detector)	2 mg – 10 mg	Changes of electron momentum of valence electrons	Lower spatial resolution compared with some of the other techniques	200 µm – 100 mm (depending on materials and X-ray energy, bulk sensitivity)	[59, 114]

The APT technique was utilized to successfully investigate the formation of the CEI layer on the surface of a $LiMn_2O_4$ (LMO) electrode.[179] The results revealed the presence of a mixed layered- and mosaic structure comprising two Mn-rich layers adsorbed onto the LMO surface and an external mosaic structure consisting primarily of LiF, Li_2O, and Li-carboxylates. Decomposition of the Li salt from the liquid electrolyte on the electrode surface began even before charge discharge cycles as shown by cryo-APT, leading to newly created grain boundaries that facilitated structural changes of the electrode at the nanoscale.[151] As structural defects assist the nucleation of Li-rich phases in subsequent lithiation and accelerate electrolyte decomposition, these insights into the interactions between the nanoscale structure and electrolyte contribute to improve the understanding of self-catalyzed/accelerated degradation of electrode materials.[151] Cryogenic specimen preparation, transport under ultra-high vacuum and air have been investigated in detail for analysis of the electrode materials.[180]

4.5. EC-MS for Studying Gas Evolution During Degradation

In EC-MS, electrochemistry is used to determine the concentration or chemical reactivity of a substance by measuring either the potential, charge, or current; and mass spectroscopy is applied to detect gaseous products generated in an electrochemical cell.[181] By utilizing a mass spectrometer, EC-MS can effectively monitor the formation of intermediate species in electrochemical reactions, identify and quantify reaction products, advance understanding of ion formation, and uncover unexpected redox reactions.[152] For example, EC-MS has been used for evaluation of electrolyte decomposition inside a battery. The mass spectrometric signals from EC-MS detected different mass/charge number (m/z) values from the cycled battery which indicated the formation of different gases and were characteristic of the electrolyte decomposition reactions.[182] At the beginning of charging of the battery, a peak corresponding to $m/z = 2$ appeared in the spectrum, indicating H_2 evolution, referring to a reductive gas formation reaction,[182] and this may occur due to trace amounts of H_2O in the electrolyte.[183] Apart from H_2, $m/z = 26$, 27, 28, and 44 also appeared at the beginning of the charge cycle, these values are referred to the formation of C_2H_4, CO, and CO_2, respectively. Almost at the end of the 1st charge cycle, a peak at $m/z = 44$ appeared, probably due to oxidative decomposition of solvent molecules in the electrolyte at higher voltages.[182] Overall, the formation of both CO_2 and H_2 was observed during 20 cycles whereas C_2H_4 was only detected in the 1st cycle, the evolution rate of H_2 remained constant, but that of CO_2 increased, this may be associated with a change in the electrode/electrolyte interfacial structure upon cycling.[182]

The on-chip EC-MS method employs a microfabricated membrane chip to regulate volatile species transfer from an electrochemical cell to a mass spectrometer, allowing instantaneous gas exchange to simulate cross-talk phenomena.[184] This study is one of the pioneering applications of EC-MS in the investigation of cathode degradation in LIBs. Additionally, the study also introduced a new cell design to enable *operando* measurements of gas evolution and gain insights into these intricate mechanisms of the impact of TM dissolution on the stability of the

anodic SEI by monitoring ethylene evolution, as well as conducting isotopic labeling studies to analyze the evolution and consumption of CO_2 generated from the cathode. Additionally, ex situ surface-sensitive analysis techniques such as XPS and ToF-SIMS were employed to obtain complementary understanding of the reactivity and chemistry evolution of LIBs during operation. The DRX cathodes follow similar redox mechanisms with O_2 evolution upon degradation. *Operando* EC-MS was also utilized to track the gas emissions of not only cathode materials but also solid-state electrolyte materials such as $Li_7La_3Zr_2O_{12}$ (LLZO).[185] By utilizing proper controls, CO_2 and O_2 were identified as emanating from the interface between the electrolyte and cathode. The gas evolution was correlated with a significant increase in cathode interfacial resistance as observed through potential-resolved impedance spectroscopy. To gain a comprehensive understanding of the intricate reactivity and chemical evolution of LIBs during operation, a combination of complementary and correlative surface sensitive analysis techniques, such as XPS and ToF-SIMS, can also be employed.

5. Conclusion and Outlook

Table 1 below summarizes the various techniques and the characteristics associated with each technique.

DRX materials hold great promise as Li-rich cathode materials for rechargeable batteries. The wider choice of TM elements and higher capacities due to the utilization of both TM and O-redox have made DRX materials attractive in terms of sustainability and advancements in performance. However, the presence of γ-$LiFeO_2$ type cation SRO impedes Li ion diffusion, reducing achievable capacities and redox kinetics. The DRX materials are also prone to degradation through irreversible O_2 loss and TM dissolution. Strategies to overcome these barriers include F incorporation, high entropy (multiple TM) modification, and surface coating of the particles. This review focuses on different types of advanced characterization techniques and combining the different complementary characterization techniques for correlative studies to jointly advance the fundamental understanding of DRX materials and their degradation mechanisms to show the effects of the strategies on performance improvements, e.g. visualizing cation SRO, Li percolation, tracking cationic/anionic redox, probing degradation mechanisms, monitoring surface reactions, and detecting F environments.

Specific perspective toward achieving deeper understanding of DRX materials using complementary characterization techniques is summarized in **Figure 16** and listed as the following:

i. The cation SRO has been visualized and quantified by STEM, nPDF, and ssNMR. These are key techniques to effectively provide deep understanding of Li concentration distributions, Li percolation, and the change of SRO in DRX upon addition/reduction of different cation types, as these mechanisms have only been previously studied by DFT and MC simulations, for limited compositional space. Future investigation on SRO visualization toward the addition/reduction of different redox centers can be an effective option to guide cathode compositional design as well as further understanding of structural evolution upon cycling.
ii. Compared to the cationic SRO, there are fewer studies on the anionic SRO in DRX. STEM with ptychography has the power of analyzing anionic SRO, owing to its ability to visualize light elements; nPDF has already been applied to the study of anion ordering. Given that different types of anions ordering in DRX and different arrangements of Li-rich environments, and hence, effective percolation in the structure, more advanced characterization can be applied to the anionic SRO studies.

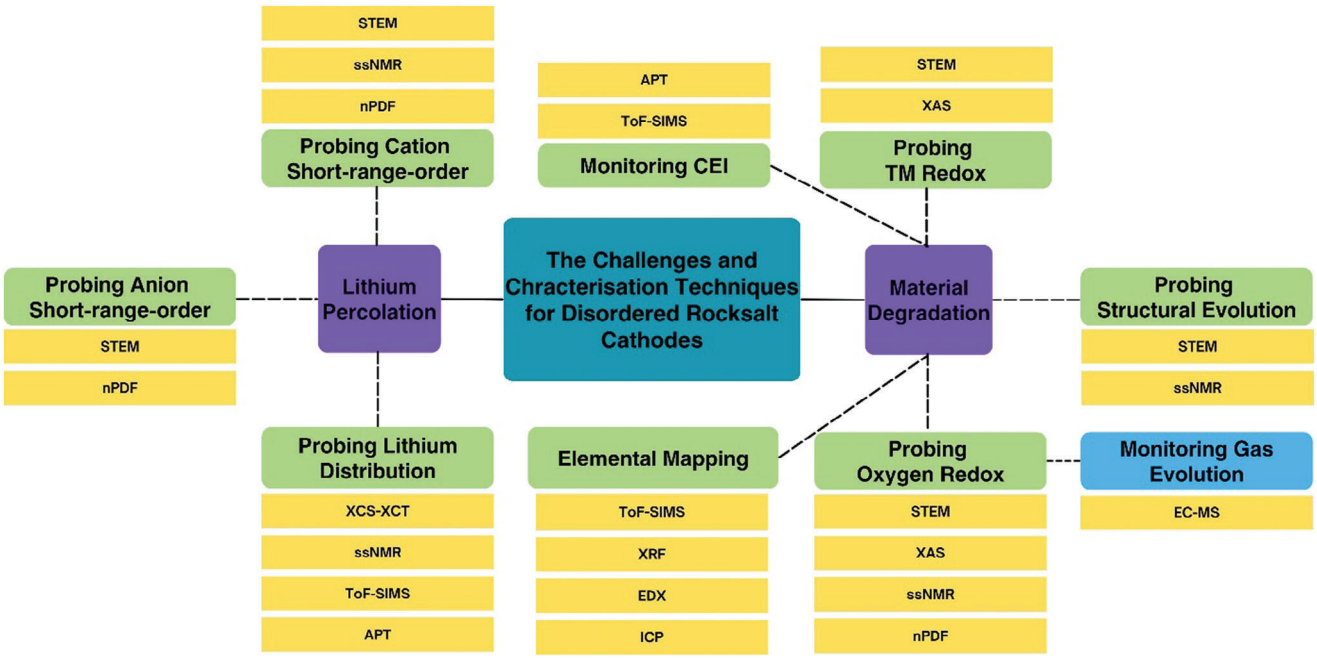

Figure 16. Connecting the challenges for DRX and future outlook for the applications of complementary characterization techniques.

iii. Li is the lightest metallic element in the periodic table, it remains challenging to characterize and monitor the Li content in DRX. ^{7}Li ssNMR allows for the investigation of local environments of Li nuclei along with the SRO studies, which gives information of the Li diffusion barrier in the DRX system. ToF-SIMS is a promising approach for the detection and quantification of Li, in which FIB prior to ToF-SIMS mapping offers direct visualization of Li distributions. In addition, *operando* correlative imaging of combining XCT and XCS imaging (XCS-I) has been used to study the Li ion diffusivity in 3D microstructures; 3D elemental distributions were also reconstructed using APT, there is a lot of space for these characterization techniques to be applied to study DRX materials.

iv. The structural evolution of DRX has been studied by HAADF-STEM and FFT, however, O-redox has been extensively investigated in the conventional layered cathodes for LIBs, but less focus on DRX materials. Direct imaging of O-shift was achieved using STEM with ptychography; RIXS, ss-NMR, and nPDF provided evidence of the nature of O_2 at both bulk and surface level. Given that the DRX cathodes follow similar redox mechanisms with O_2 evolution upon degradation, these approaches will provide unique insights into the degradation of DRX.

v. For TM redox studies, XAS-based techniques are useful for probing cation oxidation states. As a novel approach, the combined STXM-XAS provides valuable insights into the distributions of elemental compositions and oxidation states. Spatially resolved 2D- and 3D-STXM has already been applied to reveal the cationic redox pattern in a few DRX materials, but with limited compositional space so far.

vi. ToF-SIMS has been applied to observe the existence of CEI layers on the cathodes, e.g. $Li_{1.2}Mn_{0.4}Ti_{0.4}O_2$, $LiMn_{1.5}Ni_{0.5}O_4$ and $Li_{1.2}Mn_{0.6}Ni_{0.2}O_2$; APT has been used to investigate the CEI formation of LMO cathode. However, current studies on the CEI of DRX are still limited for DRX particles.

Considering ongoing progress in advanced characterization techniques, we anticipate more studies on enhancing Li ion diffusion in the DRX material crystal structures and prevention of oxygen loss and TM dissolution to improve cycling stability. In-depth understanding of the effects of different TM elements on DRX performance and degradation mechanisms will facilitate design of the material chemical compositions to encourage the use of more abundant TM elements and elimination of scarce TM elements (or TM with energy intensive production) to improve sustainability of cathode materials.

Acknowledgements

C.H. acknowledges Faraday Institution research programme grants FIRG060 and FIRG066, ERC Starting Grant (converted to UKRI funding EP/Y009908/1), UKRI EPSRC UKRI Innovation Fellowship (EP/S001239/1, EP/S001239/2), Faraday Institution Industry Fellowship (FIIF015), Faraday Institution Training Grant (FITG034) and Imperial College London UKRI Impact Acceleration Account EP/X52556X/1. C.L.A.Leung acknowledges the financial support from the UKRI EPSRC, grants numbered EP/W006774/1, EP/W003333/1, EP/V061798/1, and EP/W037483/1.

Conflict of Interest

The authors declare no conflict of interest.

Keywords

advanced characterization, cathode materials, disordered rocksalt, lithium ion batteries, lithium-excess

Received: July 15, 2023
Revised: January 18, 2024
Published online:

[1] L. Xu, T. Meng, X. Zheng, T. Li, A. H. Brozena, Y. Mao, Q. Zhang, B. C. Clifford, J. Rao, L. Hu, *Adv. Funct. Mater.* **2023**, *33*, 2302098.
[2] U.S. Geological Survey, Mineral commodity summaries **2023**, https://pubs.usgs.gov/publication/mcs2023
[3] What are Rare Earth Elements (REEs), where are they found and how are they mined?, https://etech-resources.com/what-are-rare-earth-elements-rees-where-are-they-found-and-how-are-they-mined/ (accessed: September 2021).
[4] Trading Economics **2023**, https://tradingeconomics.com/commodity.
[5] London Metal Exchange **2023**, https://www.lme.com/en/.
[6] A. Urban, J. Lee, G. Ceder, *Adv. Energy Mater.* **2014**, *4*, 1400478.
[7] J. Lee, A. Urban, X. Li, D. Su, G. Hautier, G. Ceder, *Science* **2014**, *343*, 519.
[8] D. Chen, J. Ahn, G. Chen, *ACS Energy Lett.* **2021**, *6*, 1358.
[9] R. J. Clément, Z. Lun, G. Ceder, *Energy Environ. Sci.* **2020**, *13*, 345.
[10] R. Wang, X. Li, L. Liu, J. Lee, D.-H. Seo, S.-H. Bo, A. Urban, G. Ceder, *Electrochem. Commun.* **2015**, *60*, 70.
[11] Q. Wang, A. Sarkar, D. Wang, L. Velasco, R. Azmi, S. S. Bhattacharya, T. Bergfeldt, A. Düvel, P. Heitjans, T. Brezesinski, H. Hahn, B. Breitung, *Energy Environ. Sci.* **2019**, *12*, 2433.
[12] Z. Lun, B. Ouyang, D.-H. Kwon, Y. Ha, E. E. Foley, T.-Y. Huang, Z. Cai, H. Kim, M. Balasubramanian, Y. Sun, J. Huang, Y. Tian, H. Kim, B. D. McCloskey, W. Yang, R. J. Clément, H. Ji, G. Ceder, *Nat. Mater.* **2021**, *20*, 214.
[13] Y. Chen, C. Huang, *RSC Adv.* **2023**, *13*, 29343.
[14] R. F. Ziesche, T. M. Heenan, P. Kumari, J. Williams, W. Li, M. E. Curd, T. L. Burnett, I. Robinson, D. J. Brett, M. J. M.-D. C. B. M Ehrhardt, *Adv. Energy Mater.* **2023**, *13*, 2300103.
[15] H. Ji, A. Urban, D. A. Kitchaev, D.-H. Kwon, N. Artrith, C. Ophus, W. Huang, Z. Cai, T. Shi, J. C. Kim, H. Kim, G. Ceder, *Nat. Commun.* **2019**, *10*, 592.
[16] W. H. Kan, B. Deng, Y. Xu, A. K. Shukla, T. Bo, S. Zhang, J. Liu, P. Pianetta, B.-T. Wang, Y. Liu, G. Chen, *Chem* **2018**, *4*, 2108.
[17] C. Huang, N. P. Young, J. Zhang, H. J. Snaith, P. S. Grant, *Nano Energy* **2017**, *31*, 377.
[18] B. Ouyang, N. Artrith, Z. Lun, Z. Jadidi, D. A. Kitchaev, H. Ji, A. Urban, G. Ceder, *Adv. Energy Mater.* **2020**, *10*, 1903240.
[19] J. Ahn, D. Chen, G. Chen, *Adv. Energy Mater.* **2020**, *10*, 2001671.
[20] Y. He, S. Wang, H. Zhang, X. Chen, J. Li, H. Xu, Y. Zhang, K. Hu, G. Lv, Y. Meng, W. Xiang, *J. Colloid Interface Sci.* **2022**, *607*, 1333.
[21] L. Li, Z. Lun, D. Chen, Y. Yue, W. Tong, G. Chen, G. Ceder, C. Wang, *Adv. Funct. Mater.* **2021**, *31*, 2101888.
[22] Z. Jadidi, T. Chen, P. Xiao, A. Urban, G. Ceder, *J. Mater. Chem. A* **2020**, *8*, 19965.
[23] W. D. Richards, S. T. Dacek, D. A. Kitchaev, G. Ceder, *Adv. Energy Mater.* **2018**, *8*, 1701533.
[24] N. J. Szymanski, Y. Zeng, T. Bennett, S. Patil, J. K. Keum, E. C. Self, J. Bai, Z. Cai, R. Giovine, B. Ouyang, F. Wang, C. J. Bartel, R. J. Clément, W. Tong, J. Nanda, G. Ceder, *Chem. Mater.* **2022**, *34*, 7015.

[25] W. Tang, G. Zhou, C. Hu, A. Li, Z. Chen, Z. Yang, J. Su, W. Zhang, *ACS Appl. Mater. Interfaces* **2023**, *15*, 17938.
[26] Y. He, W. Xiang, G. Lv, Y. Zhong, Y. Song, K. Zhou, Z. Wu, Zhang, E. Yang, X. Guo, *Chem. Eng. J.* **2021**, *417*, 128189.
[27] G. Assat, A. Iadecola, C. Delacourt, R. Dedryvère, J.-M. Tarascon, *Chem. Mater.* **2017**, *29*, 9714.
[28] M. A. Jones, P. J. Reeves, I. D. Seymour, M. J. Cliffe, S. E. Dutton, C. P. Grey, *Chem Commun (Camb)* **2019**, *55*, 9027.
[29] R. A. House, J.-J. Marie, M. A. Pérez-Osorio, G. J. Rees, E. Boivin, P. G. Bruce, *Nat. Energy* **2021**, *6*, 781.
[30] B. L. Rinkel, D. S. Hall, I. Temprano, C. P. Grey, *J. Am. Chem. Soc.* **2020**, *142*, 15058.
[31] C. Jayawardana, N. Rodrigo, B. Parimalam, B. L. Lucht, *ACS Energy Lett.* **2021**, *6*, 3788.
[32] W. M. Dose, I. Temprano, J. P. Allen, E. Bjorklund, C. A. O'Keefe, W. Li, B. L. Mehdi, R. S. Weatherup, M. F. De Volder, C. P. Grey, *ACS Appl. Mater. Interfaces* **2022**, *14*, 13206.
[33] C. Zhan, T. Wu, J. Lu, K. Amine, *Energy Environ. Sci.* **2018**, *11*, 243.
[34] S. Solchenbach, G. Hong, A. T. S. Freiberg, R. Jung, H. A. Gasteiger, *J. Electrochem. Soc.* **2018**, *165*, A3304.
[35] Y. Li, X.-W. Zhang, S. A. Khan, P. S. Fedkiw, *Electrochem. Solid-State Lett.* **2004**, *7*, A228.
[36] A. Gabryelczyk, S. Ivanov, A. Bund, G. Lota, *J. Energy Storage* **2021**, *43*, 103226.
[37] M. Morita, T. Shibata, N. Yoshimoto, M. Ishikawa, *J. Power Sources* **2003**, *119*, 784.
[38] Q. Liu, T. L. Dzwiniel, K. Z. Pupek, Z. Zhang, *J. Electrochem. Soc.* **2019**, *166*, A3959.
[39] H. Yang, K. Kwon, T. M. Devine, J. W. Evans, *J. Electrochem. Soc.* **2000**, *147*, 4399.
[40] S.-W. Song, T. J. Richardson, G. V. Zhuang, T. M. Devine, J. W. Evans, *Electrochim. Acta* **2004**, *49*, 1483.
[41] P. Novák, *Environmental Deterioration of Materials* (Ed: F. Escrig), WIT Press, Boston **2007**, pp. 27–71.
[42] D. H. Seo, J. Lee, A. Urban, R. Malik, S. Kang, G. Ceder, *Nat. Chem.* **2016**, *8*, 692.
[43] R. A. House, G. J. Rees, K. McColl, J.-J. Marie, M. Garcia-Fernandez, A. Nag, K.-J. Zhou, S. Cassidy, B. J. Morgan, M. Saiful Islam, P. G. Bruce, *Nat. Energy* **2023**, *8*, 351.
[44] E. McCalla, A. M. Abakumov, M. Saubanère, D. Foix, E. J. Berg, G. Rousse, M.-L. Doublet, D. Gonbeau, P. Novák, G. Van Tendeloo, R. Dominko, J.-M. Tarascon, *Science* **2015**, *350*, 1516.
[45] M. Saubanère, E. McCalla, J. M. Tarascon, M. L. Doublet, *Energy Environ. Sci.* **2016**, *9*, 984.
[46] J. Hong, W. E. Gent, P. Xiao, K. Lim, D.-H. Seo, J. Wu, P. M. Csernica, C. J. Takacs, D. Nordlund, C.-J. Sun, K. H. Stone, D. Passarello, W. Yang, D. Prendergast, G. Ceder, M. F. Toney, W. C. Chueh, *Nat. Mater.* **2019**, *18*, 256.
[47] M. Ben Yahia, J. Vergnet, M. Saubanère, M.-L. Doublet, *Nat. Mater.* **2019**, *18*, 496.
[48] J. Lee, D.-H. Seo, M. Balasubramanian, N. Twu, X. Li, G. Ceder, *Energy Environ. Sci.* **2015**, *8*, 3255.
[49] D. Chen, W. H. Kan, G. Chen, *Adv. Energy Mater.* **2019**, *9*, 1901255.
[50] R. A. House, H. Y. Playford, R. I. Smith, J. Holter, I. Griffiths, K.-J. Zhou, P. G. Bruce, *Energy Environ. Sci.* **2022**, *15*, 376.
[51] J. Burns, B. Ouyang, J. Cheng, M. K. Horton, M. Siron, O. Andriuc, R. Yang, G. Ceder, K. A. Persson, *Chem. Mater.* **2022**, *34*, 7210.
[52] Z. Cai, B. Ouyang, H.-M. Hau, T. Chen, R. Giovine, K. P. Koirala, L. Li, H. Ji, Y. Ha, Y. Sun, *Nat. Energy* **2023**, 9, 27.
[53] L. Wang, Z. He, B. Ouyang, *Comput. Mater. Sci.* **2023**, *230*, 112513.
[54] H. Huo, C. J. Bartel, T. He, A. Trewartha, A. Dunn, B. Ouyang, A. Jain, G. Ceder, *Chem. Mater.* **2022**, *34*, 7323.
[55] B. Gault, J. D. Poplawsky, *Nat. Commun.* **2021**, *12*, 3740.
[56] Y. J. Lee, F. Wang, C. Grey, *J. Am. Chem. Soc.* **1998**, *120*, 12601.
[57] J. Liu, A. Huq, Z. Moorhead-Rosenberg, A. Manthiram, K. Page, *Chem. Mater.* **2016**, *28*, 6817.
[58] G. Wang, S. Bewlay, S. A. Needham, H.-K. Liu, R. Liu, V. Drozd, J.-F. Lee, J. Chen, *J. Electrochem. Soc.* **2005**, *153*, A25.
[59] C. Huang, M. D. Wilson, K. Suzuki, E. Liotti, T. Connolley, O. V. Magdysyuk, S. Collins, F. Van Assche, M. N. Boone, M. C. Veale, *Adv. Sci.* **2022**, *9*, 2105723.
[60] D. O. Semykina, Y. A. Morkhova, A. A. Kabanov, K. V. Mishchenko, A. B. Slobodyuk, M. A. Kirsanova, O. A. Podgornova, A. A. Shindrov, K. S. Okhotnikov, N. V. Kosova, *Phys. Chem. Chem. Phys.* **2022**, *24*, 5823.
[61] W. Song, M. A. Pérez-Osorio, J.-J. Marie, E. Liberti, X. Luo, C. O'Leary, R. A. House, P. G. Bruce, P. D. Nellist, *Joule* **2022**, *6*, 1049.
[62] P. Withers, J. Donoghue, T. Burnett, *Microsc. Microanal.* **2021**, *27*, 932.
[63] P. Trimby, I. Anderson, J. Lindsay, A. Gholinia, T. Burnett, P. Withers, *Microsc. Microanal.* **2021**, *27*, 1596.
[64] R. Zhang, S. Zhao, C. Ophus, Y. Deng, S. J. Vachhani, B. Ozdol, R. Traylor, K. C. Bustillo, J. W. Morris, D. C. Chrzan, M. Asta, A. M. Minor, *Sci. Adv.* **2019**, *5*, eaax2799.
[65] P. Nan, K. Wu, Y. Liu, K. Xia, T. Zhu, F. Lin, J. He, B. Ge, *Nanoscale* **2020**, *12*, 21624.
[66] Y. Wu, F. Zhang, X. Yuan, H. Huang, X. Wen, Y. Wang, M. Zhang, H. Wu, X. Liu, H. Wang, S. Jiang, Z. Lu, *J. Mater. Sci. Technol.* **2021**, *62*, 214.
[67] Z. Lun, B. Ouyang, Z. Cai, R. J. Clément, D.-H. Kwon, J. Huang, J. K. Papp, M. Balasubramanian, Y. Tian, B. D. McCloskey, *Chem* **2020**, *6*, 153.
[68] X. Hua, T. Dean, S. A. Cussen, A. L. Goodwin, *Journal of Physics: Materials* **2023**, *6*, 045007.
[69] G. S. Henderson, F. M. F. de Groot, B. J. A. Moulton, *Reviews in Mineralogy and Geochemistry* **2014**, *78*, 75.
[70] S. J. Gurman, *J. Mater. Sci.* **1982**, *17*, 1541.
[71] L. J. P. Ament, M. van Veenendaal, T. P. Devereaux, J. P. Hill, J. van den Brink, *Rev. Mod. Phys.* **2011**, *83*, 705.
[72] J. A. van Bokhoven, C. Louis, J. T. Miller, M. Tromp, O. V. Safonova, P. Glatzel, *Angew. Chem., Int. Ed.* **2006**, *45*, 4651.
[73] C. Bressler, M. Chergui, *Chem. Rev.* **2004**, *104*, 1781.
[74] Q. Gu, J. A. Kimpton, H. E. A. Brand, Z. Wang, S. Chou, *Adv. Energy Mater.* **2017**, *7*, 1602831.
[75] P. Zimmermann, S. Peredkov, P. M. Abdala, S. DeBeer, M. Tromp, C. Müller, J. A. van Bokhoven, *Coord. Chem. Rev.* **2020**, *423*, 213466.
[76] I. E. L. Stephens, K. Chan, A. Bagger, S. W. Boettcher, J. Bonin, E. Boutin, A. K. Buckley, R. Buonsanti, E. R. Cave, X. Chang, S. W. Chee, A. H. M. da Silva, P. de Luna, O. Einsle, B. Endrődi, M. Escudero-Escribano, J. V. Ferreira de Araujo, M. C. Figueiredo, C. Hahn, K. U. Hansen, S. Haussener, S. Hunegnaw, Z. Huo, Y. J. Hwang, C. Janáky, B. S. Jayathilake, F. Jiao, Z. P. Jovanov, P. Karimi, M. T. M. Koper, et al., *J. Phys.: Energy* **2022**, *4*, 042003.
[77] G. X. Wang, S. Bewlay, S. A. Needham, H. K. Liu, R. S. Liu, V. A. Drozd, J. F. Lee, J. M. Chen, *J. Electrochem. Soc.* **2006**, *153*, A25.
[78] Y. Yue, Y. Ha, R. Giovine, R. Clément, W. Yang, W. Tong, *Chem. Mater.* **2022**, *34*, 1524.
[79] D. Chen, J. Ahn, E. Self, J. Nanda, G. Chen, *J. Mater. Chem. A* **2021**, *9*, 7826.
[80] B. E. Warren, *X-ray Diffraction*, Courier Corporation, **1990**.
[81] M. T. Hutchings, *Introduction to the characterization of residual stress by neutron diffraction*, CRC Press, Boca Raton, FL **2005**.
[82] E. Törnquist, L. Gentile, S. Prévost, A. Diaz, U. Olsson, H. Isaksson, *Sci. Rep.* **2020**, *10*, 14552.
[83] X. Wang, S. Tan, X.-Q. Yang, E. Hu, *Chin. Phys. B* **2020**, *29*, 028802.
[84] L. Zhou, Q. Wang, J. Wang, X. Chen, P. Jiang, H. Zhou, F. Yuan, X. Wu, Z. Cheng, E. Ma, *Acta Mater.* **2022**, *224*, 117490.

[85] F. X. Zhang, S. Zhao, K. Jin, H. Xue, G. Velisa, H. Bei, R. Huang, J. Y. P. Ko, D. C. Pagan, J. C. Neuefeind, W. J. Weber, Y. Zhang, *Phys. Rev. Lett.* **2017**, *118*, 205501.
[86] S. J. Billinge, *Philosophical Transactions of the Royal Society A* **2019**, *377*, 20180413.
[87] M. W. Terban, S. J. Billinge, *Chem. Rev.* **2021**, *122*, 1208.
[88] R. L. McGreevy, *J. Phys.: Condens. Matter* **2001**, *13*, R877.
[89] N. J. Szymanski, Z. Lun, J. Liu, E. C. Self, C. J. Bartel, J. Nanda, B. Ouyang, G. Ceder, *Chem. Mater.* **2023**, *35*, 4922.
[90] H. Cai, R. Chen, M. Bahri, C. J. Hawkins, M. Sonni, L. M. Daniels, J. Lim, J. A. Evans, M. Zanella, L. A. Jones, *ACS Mater. Lett.* **2023**, *5*, 527.
[91] V. F. Sears, *Neutron News* **1992**, *3*, 26.
[92] B. Jiang, C. A. Bridges, R. R. Unocic, K. C. Pitike, V. R. Cooper, Y. Zhang, D.-Y. Lin, K. Page, *J. Am. Chem. Soc.* **2020**, *143*, 4193.
[93] D. Zhang, Y. Chen, H. Vega, T. Feng, D. Yu, M. Everett, J. Neuefeind, K. An, R. Chen, J. Luo, *Advanced Powder Materials* **2023**, *2*, 100098.
[94] C. Huang, M. D. Wilson, K. Suzuki, E. Liotti, T. Connolley, O. V. Magdysyuk, S. Collins, F. Van Assche, M. N. Boone, M. C. Veale, A. Lui, R.-M. Wheater, C. L. A Leung, *Adv. Sci.* **2022**, *9*, 2105723.
[95] C. L. A. Leung, M. D. Wilson, T. Connolley, S. P. Collins, O. V. Magdysyuk, M. N. Boone, K. Suzuki, M. C. Veale, E. Liotti, F. Van Assche, A. Lui, C. Huang, *Materials Today Energy* **2023**, *31*, 101224.
[96] X. Zhang, Y. Xu, H. Zhang, C. Zhao, X. Qian, *Electrochim. Acta* **2014**, *145*, 201.
[97] S. Refly, O. Floweri, T. R. Mayangsari, A. Sumboja, S. P. Santosa, T. Ogi, F. Iskandar, *ACS Sustainable Chem. Eng.* **2020**, *8*, 16104.
[98] P. Hou, G. Li, X. Gao, *J. Mater. Chem. A* **2016**, *4*, 7689.
[99] B. Çetin, Z. Camtakan, N. Yuca, *Mater. Lett.* **2020**, *273*, 127927.
[100] C. Huang, M. Dontigny, K. Zaghib, P. S. Grant, *J. Mater. Chem. A* **2019**, *7*, 21421.
[101] B.-R. Koo, Y.-G. Lee, S. H. Lee, G.-H. An, C. Huang, *Batteries* **2022**, *8*, 181.
[102] G. Tarsoly, M. Óvári, G. Záray, *Spectrochimica Acta Part B: Atomic Spectroscopy* **2010**, *65*, 287.
[103] H. A. Lee, J. Lee, E. Kwon, D. Kim, H. O. Yoon: *Determination of fluorine concentrations using wavelength dispersive X-ray fluorescence (WDXRF) spectrometry to analyze fluoride precipitates* **2015**, *2015*, H13A.
[104] S. Jeong, D. Kim, Y.-T. Kim, H.-O. Yoon, *Spectrochimica Acta Part B: Atomic Spectroscopy* **2018**, *149*, 261.
[105] U. E. A. Fittschen, G. Falkenberg, *Anal. Bioanal. Chem.* **2011**, *400*, 1743.
[106] G. Qian, F. Monaco, D. Meng, S.-J. Lee, G. Zan, J. Li, D. Karpov, S. Gul, D. Vine, B. Stripe, J. Zhang, J.-S. Lee, Z.-F. Ma, W. Yun, P. Pianetta, X. Yu, L. Li, P. Cloeten, Y. Liu, *Cell Reports Physical Science* **2021**, *2*, 100554.
[107] H. Gao, J. Cai, G.-L. Xu, L. Li, Y. Ren, X. Meng, K. Amine, Z. Chen, *Chem. Mater.* **2019**, *31*, 2723.
[108] M. J. Cooper, in *Encyclopedia of Materials: Science and Technology* (Eds: K. H. J. Buschow, R. W. Cahn, M. C. Flemings, B. Ilschner, E. J. Kramer, S. Mahajan, P. Veyssière), Elsevier, Oxford **2001**, pp. 1453.
[109] C. Huang, C. L. A. Leung, P. Leung, P. S. Grant, *Adv. Energy Mater.* **2020**, *11*, 2002387.
[110] K. Suzuki, A. Suzuki, T. Ishikawa, M. Itou, H. Yamashige, Y. Orikasa, Y. Uchimoto, Y. Sakurai, H. Sakurai, *Journal of Synchrotron Radiation* **2017**, *24*, 1006.
[111] K. Suzuki, R. Kanai, N. Tsuji, H. Yamashige, Y. Orikasa, Y. Uchimoto, Y. Sakurai, H. Sakurai, *Condensed Matter* **2018**, *3*, 27.
[112] C. Huang, P. S. Grant, *J. Mater. Chem. A* **2018**, *6*, 14689.
[113] P. J. Withers, C. Bouman, S. Carmignato, V. Cnudde, D. Grimaldi, C. K. Hagen, E. Maire, M. Manley, A. Du Plessis, S. R. Stock, *Nature Reviews Methods Primers* **2021**, *1*, 18.
[114] C. L. A. Leung, M. D. Wilson, T. Connolley, S. P. Collins, O. V. Magdysyuk, M. N. Boone, K. Suzuki, M. C. Veale, E. Liotti, F. Van Assche, *Materials Today Energy* **2023**, *31*, 101224.
[115] T. Insinna, E. N. Bassey, K. Marker, A. Collauto, A.-L. Barra, C. Grey, *Chem. Mater.* **2023**, *35*, 5497.
[116] C. P. Grey, N. Dupré, *Chem. Rev.* **2004**, *104*, 4493.
[117] C. P. Rosenau, B. J. Jelier, A. D. Gossert, A. Togni, *Angew. Chem., Int. Ed.* **2018**, *57*, 9528.
[118] F. Castiglione, A. Mele, G. Raos, *Annual Reports on NMR Spectroscopy* **2015**, *85*, 143.
[119] I. Hung, L. Zhou, F. Pourpoint, C. P. Grey, Z. Gan, *J. Am. Chem. Soc.* **2012**, *134*, 1898.
[120] K. Märker, P. J. Reeves, C. Xu, K. J. Griffith, C. P. Grey, *Chem. Mater.* **2019**, *31*, 2545.
[121] R. J. Clément, D. Kitchaev, J. Lee, C. Gerbrand, *Chem. Mater.* **2018**, *30*, 6945.
[122] N. M. Laptash, A. A. Udovenko, *J. Struct. Chem.* **2016**, *57*, 390.
[123] R. A. House, J.-J. Marie, J. Park, G. J. Rees, S. Agrestini, A. Nag, M. Garcia-Fernandez, K.-J. Zhou, P. G. Bruce, *Nat. Commun.* **2021**, *12*, 2975.
[124] R. A. House, G. J. Rees, M. A. Pérez-Osorio, J.-J. Marie, E. Boivin, A. W. Robertson, A. Nag, M. Garcia-Fernandez, K.-J. Zhou, P. G. Bruce, *Nat. Energy* **2020**, *5*, 777.
[125] R. A. House, U. Maitra, M. A. Pérez-Osorio, J. G. Lozano, L. Jin, J. W. Somerville, L. C. Duda, A. Nag, A. Walters, K.-J. Zhou, M. R. Roberts, P. G Bruce, *Nature* **2020**, *577*, 502.
[126] J. Lee, N. Dupre, M. Avdeev, B. Kang, *Sci. Rep.* **2017**, *7*, 6728.
[127] S. Patil, D. Darbar, E. C. Self, T. Malkowski, V. C. Wu, R. Giovine, N. J. Szymanski, R. D. McAuliffe, B. Jiang, J. K. Keum, K. P. Koirala, B. Ouyang, K. Page, C. Wang, G. Ceder, R. J. Clément, J. Nanda, *Adv. Energy Mater.* **2023**, *13*, 2203207.
[128] J. Lee, J. K. Papp, R. J. Clément, S. Sallis, D.-H. Kwon, T. Shi, W. Yang, B. D. McCloskey, G. Ceder, *Nat. Commun.* **2017**, *8*, 981.
[129] V. Murugesan, J. S. Cho, N. Govind, A. Andersen, M. J. Olszta, K. S. Han, G. Li, H. Lee, D. M. Reed, V. L. Sprenkle, S. Cho, S. K. Nune, D. Choi, *ACS Appl. Energy Mater.* **2019**, *2*, 1832.
[130] D. A. Kitchaev, Z. Lun, W. D. Richards, H. Ji, R. J. Clément, M. Balasubramanian, D.-H. Kwon, K. Dai, J. K. Papp, T. Lei, B. D. McCloskey, W. Yang, J. Lee, G. Ceder, *Energy Environ. Sci.* **2018**, *11*, 2159.
[131] C. A. Evans, *Thin Solid Films* **1973**, *19*, 11.
[132] Z. Sha, Z. Shen, E. Calì, J. A. Kilner, S. J. Skinner, *J. Mater. Chem. A* **2023**, *11*, 5645.
[133] S. Bessette, A. Paolella, C. Kim, W. Zhu, P. Hovington, R. Gauvin, K. Zaghib, *Sci. Rep.* **2018**, *8*, 17575.
[134] A. Priebe, T. Xie, G. Bürki, L. Pethö, J. Michler, *J. Anal. At. Spectrom.* **2020**, *35*, 1156.
[135] M. Ohnishi, O. Matsuoka, H. Nogi, T. Sakamoto, *e-J. Surface Sci. Nanotechnol.* **2012**, *10*, 207.
[136] V. R. Rikka, S. R. Sahu, M. Gurumurthy, A. Chatterjee, S. Chandran, G. Sundararajan, R. Gopalan, R. Prakash, *Energy Technol.* **2023**, *11*, 2201388.
[137] I. V. Veryovkin, C. E. Tripa, A. V. Zinovev, S. V. Baryshev, Y. Li, D. P. Abraham, *Nuclear Instruments and Methods in Physics Research Section B: Beam Interactions with Materials and Atoms* **2014**, *332*, 368.
[138] H. Ota, T. Akai, H. Namita, S. Yamaguchi, M. Nomura, *J. Power Sources* **2003**, *119–121*, 567.
[139] C. Fiedler, B. Luerssen, M. Rohnke, J. Sann, J. Janek, *J. Electrochem. Soc.* **2017**, *164*, A3742.
[140] M. Ohnishi, O. Matsuoka, H. Nogi, T. Sakamoto, *Journal of Surface Analysis* **2013**, *20*, 99.
[141] T. Sui, B. Song, J. Dluhos, L. Lu, A. M. Korsunsky, *Nano Energy* **2015**, *17*, 254.
[142] S. Muto, K. Tatsumi, *Microscopy* **2017**, *66*, 39.

[143] S. Kumar, N. N. Ghosh, R. Chatterjee, *AIP Adv.* **2021**,*11*, 015311.
[144] N. Kuwata, M. Nakane, T. Miyazaki, K. Mitsuishi, J. Kawamura, *Solid State Ionics* **2018**, *320*, 266.
[145] S.-H. Kim, L. T. Stephenson, T. Schwarz, B. Gault, *Microsc. Microanal.* **2023**, *29*, 890.
[146] M. P. Singh, S.-H. Kim, X. Zhou, H. Kwak, A. Kwiatkowski da Silva, S. Antonov, L. S. Aota, C. Jung, Y. S. Jung, B. Gault, *Advanced Energy and Sustainability Research* **2023**, *4*, 2200121.
[147] A. Devaraj, M. Gu, R. Colby, P. Yan, C. M. Wang, J. M. Zheng, J. Xiao, A. Genc, J. G. Zhang, I. Belharouak, D. Wang, K. Amine, S. Thevuthasan, *Nat. Commun.* **2015**, *6*, 8014.
[148] B. Gault, A. Chiaramonti, O. Cojocaru-Mirédin, P. Stender, R. Dubosq, C. Freysoldt, S. K. Makineni, T. Li, M. Moody, J. M. Cairney, *Nature Reviews Methods Primers* **2021**, *1*, 51.
[149] Z. Xu, Z. Jiang, C. Kuai, R. Xu, C. Qin, Y. Zhang, M. M. Rahman, C. Wei, D. Nordlund, C.-J. Sun, X. Xiao, X.-W. Du, K. Zhao, P. Yan, Y. Liu, F. Lin, *Nat. Commun.* **2020**, *11*, 83.
[150] Y. You, A. Dolocan, W. Li, A. Manthiram, *Nano Lett.* **2019**, *19*, 182.
[151] S.-H. Kim, K. Dong, H. Zhao, A. A. El-Zoka, X. Zhou, E. V. Woods, F. Giuliani, I. Manke, D. Raabe, B. Gault, *J. Phys. Chem. Lett.* **2022**, *13*, 8416.
[152] A. P. Bruins, *TrAC Trends in Analytical Chemistry* **2015**, *70*, 14.
[153] W. Song, J. J. Marie, R. A. House, P. G. Bruce, P. D. Nellist, *Microsc. Microanal.* **2022**, *28*, 2606.
[154] W. Song, M. Osorio, J. Marie, E. Liberti, X. Luo, C. O'Leary, R. House, P. Bruce, P. Nellist, *Microsc. Microanal.* **2021**, *27*, 2724.
[155] L. Li, J. Ahn, Y. Yue, W. Tong, G. Chen, C. Wang, *Adv. Mater.* **2022**, *34*, 2106256.
[156] E. Lee, T.-U. Wi, J. Park, S.-W. Park, M.-H. Kim, D.-H. Lee, B.-C. Park, C. Jo, R. Malik, J. H. Lee, T. J. Shin, S. J. Kang, H.-W. Lee, J. Lee, D.-H. Seo, *Adv. Mater.* **2023**, *35*, 2208423.
[157] P. D. Nellist, B. C. McCallum, J. M. Rodenburg, *Nature* **1995**, *374*, 630.
[158] C. Huang, N. Grobert, A. A. Watt, C. Johnston, A. Crossley, N. P. Young, P. S. Grant, *Carbon* **2013**, *61*, 525.
[159] C. Huang, N. P. Young, P. S. Grant, *J. Mater. Chem. A* **2014**, *2*, 11022.
[160] R. Qiao, Q. Li, Z. Zhuo, S. Sallis, O. Fuchs, M. Blum, L. Weinhardt, C. Heske, J. Pepper, M. Jones, A. Brown, A. Spucces, K. Chow, B. Smith, P.-A. Glans, Y. Chen, S. Yan, F. Pan, L. F. J. Piper, J. Denlinger, J. Guo, Z. Hussain, Y.-D. Chuang, W. Yang, *Rev. Sci. Instrum.* **2017**, *88*, 033106.
[161] K. Dai, J. Wu, Z. Zhuo, Q. Li, S. Sallis, J. Mao, G. Ai, C. Sun, Z. Li, W. E. Gent, W. C. Chueh, Y.-d. Chuang, R. Zeng, Z.-x. Shen, F. Pan, S. Yan, L. F. J. Piper, Z. Hussain, G. Liu, W. Yang, *Joule* **2019**, *3*, 518.
[162] Y.-S. Liu, P.-A. Glans, C.-H. Chuang, M. Kapilashrami, J. Guo, *J. Electron Spectrosc. Relat. Phenom.* **2015**, *200*, 282.
[163] I. I. Abate, C. D. Pemmaraju, S. Y. Kim, K. H. Hsu, S. Sainio, B. Moritz, J. Vinson, M. F. Toney, W. Yang, W. E. Gent, *Energy Environ. Sci.* **2021**, *14*, 4858.
[164] C. Århammar, A. Pietzsch, N. Bock, E. Holmström, C. M. Araujo, J. Gråsjö, S. Zhao, S. Green, T. Peery, F. Hennies, *Proc. Natl. Acad. Sci. USA* **2011**, *108*, 6355.
[165] W. Eberhardt, T. Upton, S. Cramm, L. Incoccia, *Chem. Phys. Lett.* **1988**, *146*, 561.
[166] Z. Xue, J. Li, P. Pianetta, Y. Liu, *Accounts of Materials Research* **2022**, *3*, 854.
[167] M. Obst, G. Schmid, In *Electron Microscopy: Methods and Protocols* (Ed: J. Kuo), Humana Press, Totowa, NJ **2014**, pp. 757–781.
[168] E. G. Rightor, A. P. Hitchcock, H. Ade, R. D. Leapman, S. G. Urquhart, A. P. Smith, G. Mitchell, D. Fischer, H. J. Shin, T. Warwick, *J. Phys. Chem. B* **1997**, *101*, 1950.
[169] Y. Zhang, A. Hu, J. Liu, Z. Xu, L. Mu, S. Sainio, D. Nordlund, L. Li, C. J. Sun, X. Xiao, Y. Liu, F. Lin, *Adv. Funct. Mater.* **2022**, *32*, 2110502.
[170] T. Sun, G. Sun, F. Yu, Y. Mao, R. Tai, X. Zhang, G. Shao, Z. Wang, J. Wang, J. Zhou, *ACS Nano* **2021**, *15*, 1475.
[171] X. Gao, Y. H. Ikuhara, C. A. J. Fisher, R. Huang, A. Kuwabara, H. Moriwake, K. Kohama, Y. Ikuhara, *J. Mater. Chem. A* **2019**, *7*, 8845.
[172] H. Liu, J. Wang, X. Zhang, D. Zhou, X. Qi, B. Qiu, J. Fang, R. Kloepsch, G. Schumacher, Z. Liu, J. Li, *ACS Appl. Mater. Interfaces* **2016**, *8*, 4661.
[173] K. Zhou, C. Zhang, Y. Li, X. Liu, J. Liu, Z. Lun, Y. Yang, A Critical Evaluation of Interfacial Stability in Li-Excess Cation-Disordered Rock-Salt Oxide Cathode. SSRN 4327273 **2023**.
[174] Y. Li, X. Liu, D. Ren, H. Hsu, G.-L. Xu, J. Hou, L. Wang, X. Feng, L. Lu, W. Xu, Y. Ren, R. Li, X. He, K. Amine, M. Ouyang, *Nano Energy* **2020**, *71*, 104643.
[175] E. M. Erickson, W. Li, A. Dolocan, A. Manthiram, *ACS Appl. Mater. Interfaces* **2020**, *12*, 16451.
[176] F. Wu, W. Li, L. Chen, Y. Su, L. Bao, W. Bao, Z. Yang, J. Wang, Y. Lu, S. Chen, *Energy Storage Mater.* **2020**, *28*, 383.
[177] F. Walther, R. Koerver, T. Fuchs, S. Ohno, J. Sann, M. Rohnke, W. G. Zeier, J. Janek, *Chem. Mater.* **2019**, *31*, 3745.
[178] L. Van Vaeck, A. Adriaens, R. Gijbels, *Mass Spectrometry Reviews* **1999**, *18*, 1.
[179] R. Scipioni, D. Isheim, S. A. Barnett, *ECS Meeting Abstracts* **2019**, MA2019-01, 555.
[180] J. O. Douglas, M. Conroy, F. Giuliani, B. I. Gault, *Microsc. Microanal.* **2023**, *29*, 1009.
[181] A. K. Sharma, R. R. Mishra, *Mater. Sci. Technol.* **2017**, *34*, 123.
[182] B. B. Berkes, A. Jozwiuk, M. Vracar, H. Sommer, T. Brezesinski, J. r. Janek, *Anal. Chem.* **2015**, *87*, 5878.
[183] R. Imhof, P. Novák, *J. Electrochem. Soc.* **1998**, *145*, 1081.
[184] D. B. Thornton, B. Davies, S. Scott, Z. Shen, A. Aguadero, M. Ryan, I. E. L. Stephens, *ECS Meeting Abstracts*, **2022**, MA2022-01, 350.
[185] A. A. Delluva, J. Kulberg-Savercool, A. Holewinski, *Adv. Funct. Mater.* **2021**, *31*, 2103716.
[186] R. Ishikawa, S. Morishita, T. Tanigaki, N. Shibata, Y. Ikuhara, *Microscopy* **2023**, *72*, 78.
[187] T. F. Kelly, M. K. Miller, *Rev. Sci. Instrum.* **2007**, *78*, 031101.
[188] M. Chergui, *Compr. Biophys.* **2012**, *1*, 398.
[189] M. Fracchia, P. Ghigna, A. Vertova, S. Rondinini, A. Minguzzi, *Surfaces* **2018**, *1*, 138.
[190] T. Yomogida, D. Akiyama, K. Ouchi, Y. Kumagai, K. Higashi, Y. Kitatsuji, A. Kirishima, N. Kawamura, Y. Takahashi, *Inorg. Chem.* **2022**, *61*, 20206.
[191] R. A. House, P. G. Bruce, *Nat. Energy* **2020**, *5*, 191.
[192] J. van den Brink, *Quantum Materials: Experiments and Theory*.
[193] L. J. P Ament, *Ph.D. thesis*, Leiden University, The Netherlands **2010**.
[194] B. Heacock, D. Sarenac, D. Cory, M. Huber, J. MacLean, H. Miao, H. Wen, D. Pushin, *IUCrJ* **2020**, *7*, 893.
[195] K. Xu, F. Aldudak, O. Pecher, M. Braun, A. Neuberger, H. Foysi, J. S. auf der Günne, *Solid State Nucl. Magn. Reson.* **2023**, *126*, 101884.

Roujia Chen is a Ph.D. candidate under the supervision of Dr. Chun Huang at Department of Materials, Imperial College London, working on the performance enhancement of disordered rocksalt cathodes for lithium-ion batteries and sodium-ion batteries. Roujia completed Master of Chemistry (M.Chem.) degree in 2021.

Chu Lun Alex Leung, Associate Professor in Advanced Manufacturing in the Department of Mechanical Engineering, University College London (UCL) and Co-director of the Materials, Structure, and Manufacturing group at Harwell (MSM@H). Leung is a Fellow of the Institute of Materials, Minerals, and Mining (FIMMM). Leung's work specializes in using X-rays and neutron-based characterization techniques to study materials properties, and the development of next-generation sensing technologies, data analytics, and dream-beam technology. His work has been recognized by large facilities worldwide, including Diamond Light Source (DLS Annual Review 2018), European Synchrotron Radiation Facilities (ESRF) and STFC Central laser facilities (CLF).

Chun Huang is a Senior Lecturer in Energy Storage Materials at the Department of Materials, Imperial College London. She completed her Bachelor's degree in Materials Science and Engineering at Imperial College London and PhD degree in Materials Science at the University of Oxford. Her research focuses on new energy storage materials and advanced characterization techniques. She has been awarded the European Research Council (ERC) Starting Grant, the UK EPSRC Innovation Fellowship, and the Faraday Institution Industry Fellowship.